JGR Planets

RESEARCH ARTICLE
10.1029/2025JE009153

Key Points:

- Ripple bedforms are interpreted as a shallow lake environment overlaid by laminations that are interpreted as a deeper lake deposit
- The ripple bedforms are enriched in Fe, Mn, Zn, implying a chemical front promoted metal species precipitation in the lake or subsurface
- Chemical trends may indicate diagenetic addition of metals in a stratified lake environment in conditions favorable for habitability on Mars

Supporting Information:

Supporting Information may be found in the online version of this article.

Correspondence to:

P. J. Gasda,
gasda@lanl.gov

Citation:

Gasda, P. J., Kite, E. S., Thompson, L. M., Mondro, C., Dietrich, W. E., Weitz, C. M., et al. (2026). Amapari marker band metal-enrichments: Potential mechanisms and implications for surface and subsurface water and weathering in Gale crater. *Journal of Geophysical Research: Planets*, *131*, e2025JE009153. https://doi.org/10.1029/2025JE009153

Received 22 APR 2025
Accepted 14 MAR 2026

Author Contributions:

Conceptualization: P. J. Gasda, E. S. Kite, L. M. Thompson, C. Mondro, W. E. Dietrich, C. M. Weitz, B. Tutolo, W. H. Farrand, E. Hausrath, A. Cowart, N. L. Lanza, K. W. Lewis, S. Gupta,

Amapari Marker Band Metal-Enrichments: Potential Mechanisms and Implications for Surface and Subsurface Water and Weathering in Gale Crater

P. J. Gasda[1], E. S. Kite[2], L. M. Thompson[3], C. Mondro[4], W. E. Dietrich[5], C. M. Weitz[6], B. Tutolo[7], W. H. Farrand[8], E. Hausrath[9], A. Cowart[6], N. L. Lanza[1], K. W. Lewis[10], S. Gupta[11], A. Roberts[11], W. Goetz[12], H. E. Newsom[13], L. Crossey[13], J. Lightholder[14], C. Hardgrove[14], J. Schieber[15], S. P. Schwenzer[16], S. J. VanBommel[17], S. Schröder[18], C. D. O'Connell-Cooper[3], D. Das[1], D. Rubin[19], W. Rapin[20], T. F. Bristow[21], E. Rampe[22], P. D. Archer Jr[22], C. Seeger[4], G. Caravaca[23], J. R. Johnson[24], S. Le Mouélic[25], J. A. Grant[26], J. Davis[11], J. Lasue[20], A. Yingst[6], A. B. Bryk[5], M. P. Lamb[4], W. W. Fischer[4], C. House[27], E. Dehouck[28], A. Essunfeld[1], R. Milliken[29], R. Sheppard[6], M. Minitti[30], D. Ming[22], S. Simpson[31], J. Frydenvang[31], R. M. E. Williams[6], R. Arvidson[17], R. Gellert[32], O. Gasnault[20], S. M. Clegg[1], D. Delapp[1], A. R. Vasavada[33], and A. Fraeman[33]

[1]Los Alamos National Laboratory, Los Alamos, NM, USA, [2]Department of the Geophysical Sciences, University of Chicago, Chicago, IL, USA, [3]Department of Earth Sciences, Planetary and Space Science Centre, University of New Brunswick, Fredericton, NB, Canada, [4]Division of Geological and Planetary Sciences, California Institute of Technology, Pasadena, CA, USA, [5]Earth and Planetary Science, University of California, Berkeley, CA, USA, [6]Institut d'Astrophysique Spatiale, Université Paris-Saclay, CNRS, Orsay, France, [7]Department of Earth, Energy, and Environment, University of Calgary, Calgary, AB, Canada, [8]Space Science Institute, Boulder, CO, USA, [9]Department of Geoscience, University of Nevada-Las Vegas, Las Vegas, NV, USA, [10]Earth and Planetary Sciences, Johns Hopkins University, Baltimore, MD, USA, [11]Department of Earth Science and Engineering, Imperial College, London, UK, [12]Department of Planetary Science, Max Planck Institute for Solar System Research, Göttingen, Germany, [13]Institute of Meteoritics, The University of New Mexico, Albuquerque, NM, USA, [14]School of Earth and Space Exploration, Arizona State University, Tempe, AZ, USA, [15]Department of Earth and Atmospheric Sciences, Indiana University, Bloomington, IN, USA, [16]AstrobiologyOU, EEES, The Open University, Milton Keynes, UK, [17]McDonnell Center for the Space Sciences, Department of Earth, Environmental, and Planetary Sciences, Washington University in St. Louis, St. Louis, MO, USA, [18]German Aerospace Center (DLR), Institute of Optical Sensor Systems, Berlin, Germany, [19]Department of Earth and Planetary Sciences, University of California, Santa Cruz, CA, USA, [20]Institut de Recherche en Astrophysique et Planétologie, Université de Toulouse, CNRS, CNES, Toulouse, France, [21]Exobiology Branch, NASA Ames Research Center, Moffett Field, CA, USA, [22]Amentum, NASA Johnson Space Center, Houston, TX, USA, [23]Laboratoire Géosciences Environnement Toulouse, UMR 5563, CNRS, IRD, CNES, Université de Toulouse, Toulouse, France, [24]Johns Hopkins University Applied Physics Laboratory, Laurel, MD, USA, [25]Laboratoire de Planétologie et Géosciences, CNRS UMR 6112, Nantes Université, Université d'Angers, Le Mans Université, Nantes, France, [26]Center for Earth and Planetary Studies, National Air and Space Museum, Smithsonian Institution, Washington, DC, USA, [27]Department of Geosciences, Pennsylvania State University, University Park, PA, USA, [28]Université Claude Bernard Lyon 1, ENS de Lyon, CNRS, UJM, LGL-TPE, UMR 5276, Villeurbanne, France, [29]Department of Earth, Environmental and Planetary Sciences, Brown University, Providence, RI, USA, [30]Framework, Silver Spring, MD, USA, [31]Texas State University–Amentum Johnson Space Center Engineering, Technology, and Science II, NASA Johnson Space Center, Houston, TX, USA, [32]Department of Physics, University of Guelph, Guelph, ON, Canada, [33]Jet Propulsion Laboratory, California Institute of Technology, Pasadena, CA, USA

Abstract NASA's *Curiosity* rover is exploring a 5 km tall sedimentary mound that is hypothesized to record the transition from a warm and wet (phyllosilicate-rich) to a cold and drier (sulfate-rich) Mars. Evidence of magnesium sulfate-bearing rock has shown that *Curiosity* has crossed through this phyllosilicate-sulfate transition. Recently, *Curiosity* arrived at the Amapari Marker Band, a darker, indurated unit that can be traced laterally for tens of kilometers in orbiter images. Here, *Curiosity* found evidence for a very broad lake, and bedforms interpreted as wave-ripple laminated sedimentary rock that likely was deposited in shallow water in the explored location, before becoming a deeper lake. These rocks are enriched in Fe, Mn, and Zn which has major implications for groundwater paleohydrology in Gale crater. Three formation hypotheses are considered: concretion formation during early diagenetic alteration of shallow lake sediments, laterization or leaching of the sediments, and addition of Fe, Mn, and Zn by a mildly acidic and reducing groundwater interacting with a redox and/or pH front in a stratified lake. The preferred interpretation of the metal enrichments within the Amapari Marker band sedimentary rocks is that they formed in a shallow water environment at a redox and/or pH front within the ripple unit, which drove precipitation and concentration of metals. If the enrichments are due to

A. Roberts, W. Goetz, H. E. Newsom, L. Crossey, C. Hardgrove, J. Schieber, S. P. Schwenzer, S. J. VanBommel, S. Schröder, C. D. O'Connell-Cooper, D. Rubin, W. Rapin, T. F. Bristow, E. Rampe, P. D. Archer Jr, C. Seeger, G. Caravaca, J. R. Johnson, S. Le Mouélic, J. A. Grant, J. Davis, J. Lasue, A. Yingst, A. B. Bryk, M. P. Lamb, W. W. Fischer, C. House, E. Dehouck, A. Essunfeld, R. Milliken, R. Sheppard, M. Minitti, D. Ming, S. Simpson, J. Frydenvang, R. M. E. Williams, R. Arvidson, R. Gellert, O. Gasnault, A. R. Vasavada, A. Fraeman

Data curation: P. J. Gasda, S. Schröder, D. Das, A. Essunfeld, S. M. Clegg, D. Delapp

Formal analysis: P. J. Gasda, E. S. Kite, L. M. Thompson, C. Mondro, W. E. Dietrich, B. Tutolo, W. H. Farrand, E. Hausrath, A. Cowart, K. W. Lewis, S. Gupta, A. Roberts, W. Goetz, H. E. Newsom, L. Crossey, J. Lightholder, C. Hardgrove, S. P. Schwenzer, S. J. VanBommel, S. Schröder, C. D. O'Connell-Cooper, D. Das, W. Rapin, T. F. Bristow, E. Rampe, P. D. Archer Jr, C. Seeger, G. Caravaca, J. R. Johnson, S. Le Mouélic, J. Davis, A. B. Bryk, E. Dehouck, A. Essunfeld, S. Simpson, J. Frydenvang, R. M. E. Williams, R. Gellert, O. Gasnault, S. M. Clegg

Funding acquisition: A. R. Vasavada, A. Fraeman

Investigation: P. J. Gasda, E. S. Kite, L. M. Thompson, C. Mondro, W. E. Dietrich, C. M. Weitz, B. Tutolo, W. H. Farrand, E. Hausrath, A. Cowart, N. L. Lanza, K. W. Lewis, S. Gupta, A. Roberts, W. Goetz, H. E. Newsom, C. Hardgrove, J. Schieber, S. P. Schwenzer, S. J. VanBommel, S. Schröder, C. D. O'Connell-Cooper, D. Das, D. Rubin, W. Rapin, T. F. Bristow, E. Rampe, P. D. Archer Jr, C. Seeger, G. Caravaca, J. R. Johnson, S. Le Mouélic, J. A. Grant, J. Davis, J. Lasue, A. Yingst, A. B. Bryk, M. P. Lamb, C. House, E. Dehouck, A. Essunfeld, R. Milliken, R. Sheppard, M. Minitti, D. Ming, S. Simpson, J. Frydenvang, R. M. E. Williams, R. Arvidson, R. Gellert, O. Gasnault, A. R. Vasavada, A. Fraeman

Methodology: P. J. Gasda, E. S. Kite, L. M. Thompson, C. Mondro, B. Tutolo, W. H. Farrand, E. Hausrath, W. Goetz, L. Crossey, J. Lightholder, C. Hardgrove, S. P. Schwenzer, S. J. VanBommel, S. Schröder, T. F. Bristow, E. Rampe, P. D. Archer Jr, J. R. Johnson, A. Essunfeld, S. M. Clegg

Project administration: N. L. Lanza, T. F. Bristow, E. Rampe, P. D. Archer Jr, M. Minitti, R. Gellert, O. Gasnault, A. R. Vasavada, A. Fraeman

Resources: S. M. Clegg

Software: B. Tutolo, W. H. Farrand, W. Goetz, J. Lightholder, C. Hardgrove, S. Schröder, J. R. Johnson, A. Essunfeld, S. M. Clegg, D. Delapp

groundwater alteration, these processes could link subsurface and surface environments. Water and the presence of high amounts of redox sensitive elements and other metals are favorable indicators for habitability.

Plain Language Summary A surprisingly high amount of manganese, iron, and zinc were discovered in Gale crater, Mars by the NASA *Curiosity* rover mission in late 2022. These metals were found in preserved ripple beds that indicate a very shallow lake was once present at this location. What is most surprising about this discovery is that the rover was exploring rocks that were deposited during this time period on Mars where the climate was changing from wet to dry. The rocks just below the layers with preserved ripples are indicative of drier conditions persisting on the surface of Mars. This shallow lake formed as at least part of a deposit that spans most of the sedimentary rock mound within the crater, that became deeper over time. A deep lake such as this one can have chemical gradients and would have favorable conditions for life.

1. Introduction

The NASA Mars Science Laboratory mission with its *Curiosity* rover is exploring northwestern Aeolis Mons (informally named "Mount Sharp") within Gale crater, on Mars (5°S 138°E, ~150 km diameter; Vasavada, 2022). One goal of the mission is to better understand the martian climatic transition from a wetter and perhaps warmer early Mars to today's cold and arid planet (Grotzinger et al., 2012). The mission's primary goal is to understand the habitability of ancient Mars—whether organisms could live and thrive in the environment—and a focus of the current extended mission is to understand for how long habitable conditions may have persisted on Mars' surface or subsurface despite the increasing aridity. The *Curiosity* science team concluded that ancient Gale crater was a wet environment that was once habitable (Grotzinger et al., 2014; Vasavada, 2022). The sedimentary rocks within Gale crater have been altered extensively by both early and late diagenesis, suggesting a long-lived hydrologic system in the crater (e.g., Achilles et al., 2020; Berger et al., 2022; Gasda et al., 2022; Gasda, Lanza, et al., 2024; Martin et al., 2017).

Mount Sharp is a 5-km tall, ~80 km wide sedimentary mound. Orbital spectroscopic remote sensing of Mount Sharp along *Curiosity's* traverse identified three locations of interest: a hematite-bearing ridge (since renamed Vera Rubin ridge, VRR; Fraeman et al., 2020), a phyllosilicate-bearing trough above VRR (since renamed Glen Torridon; Bennett et al., 2023), and an overlying Mg sulfate-bearing unit currently being explored by the rover at the time of this publication containing a prominent dark-toned, erosion-resistant layer named the Amapari "Marker Band" (AMB; Figure 1; Milliken et al., 2010; Mondro, Grotzinger, et al., 2025; Rapin et al., 2021; Weitz et al., 2022). This phyllosilicate-to-evaporite sequence may record the transition of the climate of Mars from wet to dry (Bibring et al., 2006; Grotzinger et al., 2012; Meyer et al., 2025; Milliken et al., 2010). *Curiosity* landed near the base of Mount Sharp and has since explored ~30 km laterally and ~750 m vertically through fluvial, deltaic, lacustrine, and eolian sedimentary rocks (Banham et al., 2018; Edgar et al., 2020; Grotzinger et al., 2015) and had been exploring the Mg sulfate-bearing Mirador formation when the Amapari Marker Band was encountered (Figure 1b). Occasional observations of sedimentary features in the otherwise sulfate and eolian dominated Mirador formation have been interpreted as being caused by brief aqueous episodes: polygonal textures that are interpreted as forming in a wet-dry cycling environment (Rapin, Dromart, Clark, et al., 2023), and ripple bedforms interpreted as shallow water forming among dunes (Caravaca et al., 2025; Gupta et al., 2023). Prior to the arrival in the Mirador formation, the rover observed sedimentary rocks of the Mount Sharp group with mineralogy that includes unaltered components (plagioclase and pyroxene), altered components (e.g., phyllosilicate and hematite), chemical precipitates (e.g., sulfates), and amorphous material (Achilles et al., 2020). The elemental composition of the lower Murray and Carolyn Shoemaker formations of Mount Sharp group (Figure 1b) is that of a moderately altered basaltic composition, plus a sulfur component (Dehouck et al., 2022; Frydenvang et al., 2020; Thompson et al., 2020).

2. Geological Context

The AMB has been studied from orbit and using long-distance rover images (Figure 1) since solar day (sol) 3042. It is a dark-toned, erosion-resistant layer that hosts well-preserved layering, fractures, and impact craters, and that crops out on the northwest, southwest, and southeast sides of Mount Sharp (Rapin et al., 2021; Weitz et al., 2022). The entire AMB has a 1°–5° dip radially away from the center of Mount Sharp and is inferred to be continuous

Supervision: N. L. Lanza, T. F. Bristow, E. Rampe, P. D. Archer Jr, M. Minitti, R. Gellert, O. Gasnault, A. R. Vasavada, A. Fraeman
Visualization: P. J. Gasda, C. Mondro, B. Tutolo, W. H. Farrand, S. Gupta, L. Crossey, J. Lightholder, C. Hardgrove, G. Caravaca, J. R. Johnson, S. Le Mouélic, A. Essunfeld
Writing – original draft: P. J. Gasda, E. S. Kite, L. M. Thompson, C. Mondro, W. E. Dietrich, C. M. Weitz, B. Tutolo, W. H. Farrand, E. Hausrath, A. Cowart, N. L. Lanza, K. W. Lewis, S. Gupta, A. Roberts, W. Goetz, H. E. Newsom, L. Crossey, C. Hardgrove, J. Schieber, S. P. Schwenzer, S. J. VanBommel, S. Schröder, C. D. O'Connell-Cooper, D. Das, D. Rubin, W. Rapin, T. F. Bristow, E. Rampe, P. D. Archer Jr, C. Seeger, G. Caravaca, J. R. Johnson, S. Le Mouélic, J. A. Grant, J. Davis, J. Lasue, A. Yingst, A. B. Bryk, M. P. Lamb, E. Dehouck, A. Essunfeld, R. Milliken, R. Sheppard, M. Minitti, D. Ming, S. Simpson, J. Frydenvang, R. M. E. Williams, R. Arvidson, R. Gellert, O. Gasnault, A. R. Vasavada, A. Fraeman
Writing – review & editing: P. J. Gasda, E. S. Kite, L. M. Thompson, C. Mondro, W. E. Dietrich, C. M. Weitz, B. Tutolo, W. H. Farrand, A. Cowart, L. Crossey, C. Hardgrove, S. P. Schwenzer, S. J. VanBommel, S. Schröder, G. Caravaca, J. R. Johnson, A. B. Bryk, A. Essunfeld, O. Gasnault, A. R. Vasavada

over 80 km within sedimentary strata of Mount Sharp (i.e., not in the central uplift; Weitz et al., 2022). Orbital spectroscopy returned a strong high-Ca pyroxene absorption associated with the layer (Weitz et al., 2022). Based on the remote sensing analyses, the initial hypotheses proposed for the formation of the AMB prior to *Curiosity's* arrival that are consistent with its location within the sulfate-bearing strata, including: an indurated sulfate unit (either during deposition or diagenesis), a resistant sandstone, a volcanic ash deposit, or a lag deposit (Rapin et al., 2021; Weitz et al., 2022). Weitz et al. (2022) suggested that a more indurated version of the underlying sulfate materials, or an indurated volcanic ash deposit were the most likely scenarios, with a primary origin favored over a diagenetic one owing to the AMB's thin and laterally extensive nature.

The rover entered Marker Band Valley (MBV) from the north on sol 3567 (Figures 1a and 2a). The rover crossed the AMB for the first time on sol 3645 ("first crossing" Figure 1a) to briefly explore overlying western strata before returning to MBV for further inspection on sols 3669 to 3689 and crossing the AMB a second time on sols 3708 to 3774 ("second crossing" Figure 1a). Attempts to drill the erosion-resistant AMB did not succeed due to the combination of overall resistance to drilling (i.e., "hardness") and the presence of alternating recessive and resistant beds that frustrated the rover's drilling control algorithms. Drilling was successful within the thickly laminated AMB strata at Tapo Caparo. In Tapo Caparo, the rover observed the highest amounts of siderite discovered in the crater so far, and the major mineralogy includes plagioclase, pyroxene, minor or trace amounts of kieserite, bassanite, anhydrite, and a significant amorphous component (Tutolo et al., 2025).

2.1. Catrimani and Contigo Members

The AMB is a member in the primarily sulfate-bearing Mirador formation, and the AMB occurs ~200 m above the phyllosilicate-bearing lake sediments in the Mount Sharp group (Figure 1). Over this phyllosilicate-to-sulfate transition region, the dominant paleodepositional process has changed from lacustrine to eolian (e.g., Gupta et al., 2023; Mondro, Grotzinger, et al., 2025; Roberts et al., 2025). Sulfate content had increased over the course of the rover's ascent through the Mirador formation while phyllosilicates have decreased, and the fine-scale chemical content of the sediments had become increasingly variable (e.g., Rapin, Dromart, Schieber, et al., 2023). Shortly before *Curiosity* encountered the first AMB rocks on sol 3642, drill-based sampling of the Canaima target within the Contigo member confirmed the presence of hydrated crystalline Mg sulfate (Chipera et al., 2023; Figure 1).

Just below the AMB is the Catrimani member of the Mirador formation (planar bedded with a strong diagenetic overprint) above $MgSO_4$-enriched cross stratified sandstone Contigo member (Chipera et al., 2023; Roberts et al., 2025). The AMB itself is termed the Amapari member (Mondro, Grotzinger, et al., 2025). The contact between the Amapari and Catrimani members is sharp and varies in slope direction and magnitude suggesting local swales and ridges perhaps due to differential erosion or compaction (Dietrich et al., 2023), with pinch-out of the ripple unit observed in ChemCam long-distance remote micro imager (LDRMI) observations, suggesting differential erosion and scour (Dietrich et al., 2023). There is a spectroscopically distinct zone just below the AMB (up to 50 cm thick), often appearing bleached or reddish (one example shown in Figures 2h and 2i is redder than bedrock above or below it), but not chemically distinct from Catrimani bedrock (e.g., Curupira target), and with an irregular basal margin (Dietrich et al., 2023; Farrand et al., 2025). Together, these observations suggest a period of nondeposition between the Catrimani and Amapari member (Dietrich et al., 2023; Farrand et al., 2025; Mondro, Grotzinger, et al., 2025). In addition, the planar bedded stratigraphy both below and above the AMB is interpreted as forming in a sand sheet environment (Roberts et al., 2025). Sand sheet environments suggest a shallow and/or fluctuating water table was present during the deposition of the eolian material above and below the AMB. One interpretation of the AMB sedimentology is that a rising water table intersected the surface to form a lake (Mondro, Grotzinger, et al., 2025; Roberts et al., 2025).

In the Contigo member, S and Mg are abundant and well-correlated in both Alpha Particle X-Ray Spectrometer (APXS) and ChemCam observations, with correlations of S versus Fe and S versus Ca also present (Berger et al., 2024; Rapin, Dromart, Schieber, et al., 2023; Thompson et al., 2024). The abundant Ca sulfate veins observed in targets earlier in the mission (e.g., Gasda et al., 2022; Kronyak et al., 2019; VanBommel et al., 2016), are absent in the Contigo member. ChemCam, with its 500-μm spot size, does not see evidence for strong sulfate-content variations at the mm-scale, suggesting the sulfate is uniform and pervasive within the bedrock at this scale (Rapin, Dromart, Schieber, et al., 2023). These observations were consistent with the detection of crystalline Mg sulfates for the first time in Gale crater in the Canaima drill sample which is in the center of MBV (Chipera et al., 2023). The sulfate content decreases in the Catrimani member just below the AMB (Thompson et al., 2024).

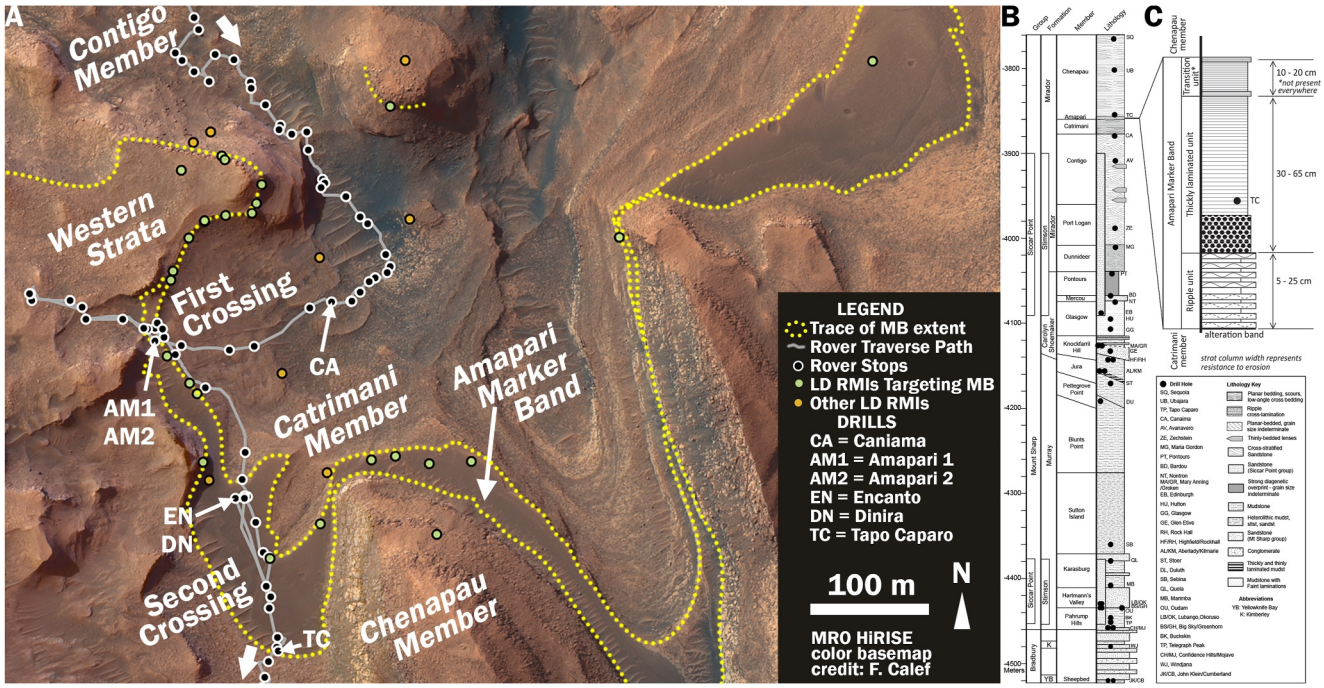

Figure 1. (a) Labeled map of the Amapari "Marker Band" region on the MRO color HiRISE basemap with the approximate extent of the AMB mapped by Mastcam and ChemCam's long-distance remote micro imager outlined (yellow dotted line). (b) Summarized stratigraphic column of the MSL traverse (Mondro, Grotzinger, et al., 2025). (c) Summary stratigraphic column of the AMB (Mondro, Grotzinger, et al., 2025).

2.2. The Amapari Member

2.2.1. Sedimentology and Stratigraphy of the AMB

The Amapari member is ~50 cm thick and comprised of two units of variable stratigraphic thickness: a lower rippled unit (5–25 cm), and an upper thickly laminated unit (30–60 cm). In some locations, a third transitional unit (10–20 cm) containing thin laminations are observed at the top of the AMB (Figures 1c, 2b–2d, and 2f; Gupta et al., 2023; Mondro, Grotzinger, et al., 2025). The basal 10 cm of the thickly laminated unit contains a dense nodular texture that is typically more erosion-resistant than the rest of the laminated unit (Figures 1c, 2b, 2e, and 2f; Gupta et al., 2023; Mondro, Grotzinger, et al., 2025). Stratigraphically, the Tapo Caparo drill location is near the bottom of the AMB thickly laminated unit and may represent a gradual transition or mixing of compositional signatures (Mondro, Grotzinger, et al., 2025). Beyond MBV, rover images show that the thickness varies, and the elevation of the AMB surface undulates by 10s of meters on the kilometer scale, with a total relief of ~100 m along the northwest side of Mount Sharp (Dietrich et al., 2023).

The very well-preserved ripple unit is composed of alternating resistant and recessive beds (Figures 1c, 2b, 2d, and 2f; Gupta et al., 2023; Mondro, Grotzinger, et al., 2025). The AMB ripple beds form hard rock plates that overhang the lower Catrimani member in places (Figure 2b). While parked on top of the AMB, materials were observed with ropey textures and the distance between these resistant features are approximately the same as the wavelength of the ripples; likely these are remnant ripple forms (Figure 2c). The rippled sedimentary structures in the lower AMB are best interpreted as wave ripples deposited in a shallow lake (Allen, 1997; Boersma, 1970; Gupta et al., 2023; Mondro, Fedo, et al., 2025; Mondro, Grotzinger, et al., 2025; Reineck & Singh, 1980). The short ripple wavelength observed (~5 cm) is consistent with no more than 2 m deep water where ripples form by wind-generated waves with no ice covering the lake (Gupta et al., 2023; Mondro, Fedo, et al., 2025; Mondro, Grotzinger, et al., 2025). Alternating resistant and recessive layers may indicate grain size variations corresponding to changing energy conditions (Gupta et al., 2023; Mondro, Fedo, et al., 2025; Mondro, Grotzinger, et al., 2025).

The laminated unit above the ripple unit, including the nodular section, may have formed as the lake became deeper over time (Mondro, Grotzinger, et al., 2025). If the AMB is a single Mount Sharp-spanning deposit as

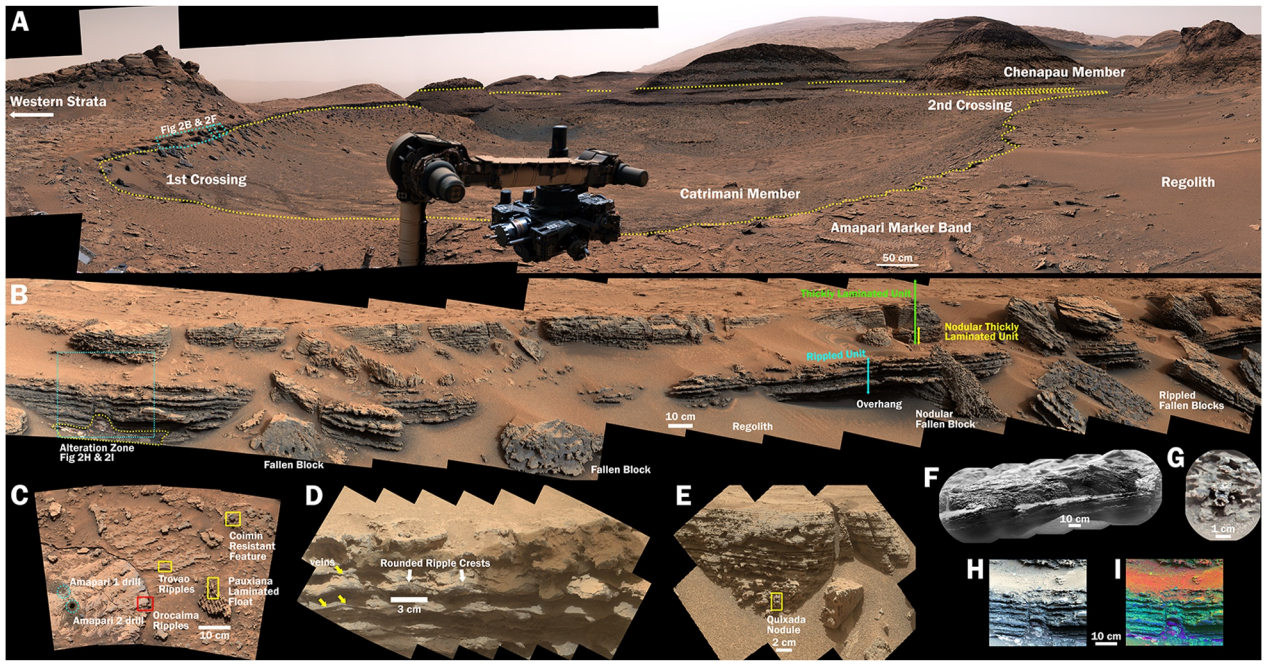

Figure 2. (a) Labeled cropped Mastcam 360 Image of Marker Band Valley at the Amapari drill site from sol 3684. The view is centered in the eastward facing direction. The approximate extent of the lower margin of Amapari "Marker Band" (AMB) as mapped by Mastcam and long-distance remote micro imager (LDRMIs) outlined (yellow dotted line). (b) Labeled Mastcam mosaic of the Marker Band outcrop at the first crossing from sol 3642 (see Figure 1). Different units of the AMB are labeled (see Figure 1c). (c) Top-down Mastcam view of the rippled layers of the AMB at the Amapari drill site from sol 3682. Selected targets are labeled as representative of different AMB units (drill targets outlined in blue, ChemCam targets outlined in yellow, and the Alpha Particle X-Ray Spectrometer target is outlined in red). (d) Labeled MAHLI close-up of the ripple unit (Mixiguana target sol 3644). (e) MAHLI mosaic of the nodular section of the thickly laminated unit (Wapixana target sol 3689). The ChemCam nodule target Quixada is labeled. (f) ChemCam long-distance remote micro imager of well-exposed AMB stratigraphy from sol 3637. (g) ChemCam RMI, colorized with Mastcam, of Quixada nodule target (sol 3688). (h) Mastcam single-frame colored-corrected image from sol 3642 of the alteration zone beneath the AMB (b, cyan box). (i) Mastcam single-frame decorrelation stretch from sol 3642 of the alteration zone (purple color) beneath the AMB (shares same scale bar with h). Mastcam image credit: NASA/JPL-Caltech/MSSS.

suggested by orbital data (Weitz et al., 2022), then the range in its topographic elevation suggests a lake up to 1.5 km deep (Dietrich et al., 2023), with a ∼100 m deep lake predicted at the location explored with the rover (Mondro, Grotzinger, et al., 2025). Within many of the thickly laminated unit outcrops, spherical features are present; centimetric features are more common near the base of this unit (Figures 2b, 2e, 2f, and 2g). These features are perhaps rounded nodules with voids/hollows, or assemblages of smaller rounded grains. The problem with a very large lake is this would require a rising lake level and a climbing shoreline to generate shallow water wave ripples up the entire 1.5 km of elevation change (Dietrich et al., 2023). Alternatively, because we have no evidence and cannot assume that there are other rippled rocks beyond what we have explored with the rover, is that MBV represents a regional low in the topography, and the shallow water that initially accumulated at this location deepened to cover the rest of the Marker Band outcrop (Mondro, Grotzinger, et al., 2025). Another option is that post-depositional differential compaction (Gabasova & Kite, 2018; Grotzinger et al., 2015) or post-depositional basement tectonics (Nimmo & Tanaka, 2005) might be responsible for this range in elevation. These two hypotheses are in tension with quantitative models that predict insufficient post-depositional tilting to account for the observations, which may require more compaction than what can be sourced by mineral bound water and pore space available in Gale materials (Dietrich et al., 2023).

2.2.2. APXS Chemistry of the AMB

At the base of the AMB, the rover's APXS instrument observed an abrupt change in chemistry compared to sedimentary rock just below the AMB (Figure 3; Table 1; Gellert, 2012; Thompson et al., 2024): evidence for sulfate enrichment (relative to the mission average) disappeared and FeO_T, MnO, and Zn greatly increased (Table 1; Gellert, 2012; Thompson et al., 2024). The ripple unit targets have the highest metal enrichments ever observed for sedimentary rocks at Gale for APXS: up to 47.51 wt.% FeO_T, 1.51 wt.% MnO, and 2.2 wt.% Zn

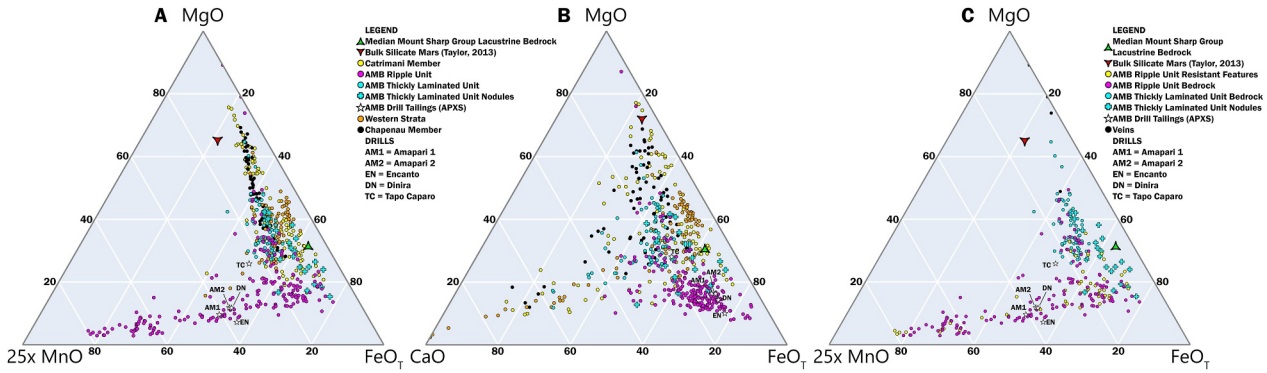

Figure 3. (a) MgO-MnOx25-FeO$_T$ ternary diagram of Marker Band Valley (MBV) member uncorrected molar ChemCam data with Alpha Particle X-Ray Spectrometer (APXS) drill tailing data (ChemCam points with >20 wt.% CaO removed) compared to bulk silicate Mars (Taylor, 2013) and the median Mount Sharp group Lacustrine bedrock ChemCam composition. (b) MgO-CaO-FeO$_T$ ternary diagram of MBV member uncorrected molar ChemCam data with APXS drill tailing data. Parts (a) and (b) share the same legend. (c) MgO-MnOx25-FeO$_T$ ternary diagram of only Marker Band uncorrected molar ChemCam data plotted by type with APXS drill tailing data (ChemCam points with >20 wt.% CaO removed).

(Gellert, 2012; Thompson et al., 2024). No increase in Ni was observed by APXS (Gellert, 2012; Thompson et al., 2024). APXS data at the second crossing again showed high FeO$_T$, Zn, and MnO, consistent with the first crossing (Gellert, 2012; Thompson et al., 2024). However, enrichments determined by APXS in Br (0.4 wt.%) and Cl (~3 wt.%) observed at the first crossing did not persist at the second crossing (Table 1; Gellert, 2012; Thompson et al., 2024). Cu enrichment was observed by APXS in drill fines for Amapari 1 and 2, but the AMB was not found to be enriched in Cu as a whole (Thompson et al., 2024). In the ripple beds, a Mn-Zn correlation is observed by APXS, but Fe-Mn and Fe-Zn are not well-correlated (Thompson et al., 2024). Within nodule targets, APXS observed a strong Fe-Zn correlation, while MnO was not enriched (Thompson et al., 2024; Figure 3c). Lastly, there is no significant correlation with, or enrichment of, P in the ripple unit (Table 1; Thompson et al., 2024) and enrichments of Pb were not reported for the AMB. The thickly laminated unit is closer to a mafic composition, similar to the average Mars crust, with slightly elevated FeO$_T$, MnO, and Zn content, but significantly less so than in the ripple unit (Thompson et al., 2024). The Tapo Caparo drill is distinct from the four other drill attempts, with lower metal content and higher sulfur content compared to the AMB drill tailings (Table 1; Thompson et al., 2024; Gellert, 2012).

3. Methods

The data presented here combines ChemCam data (Clegg et al., 2017; Maurice et al., 2012; R. Wiens, 2021a, 2021b, 2021c, 2021d; R. C. Wiens et al., 2012), rover images from Mastcam (Malin, 2021a, 2021b; Malin et al., 2017), and Mars Hand Lens Imager (MAHLI; Edgett et al., 2015), Dynamic Albedo of Neutrons (DAN; Mitrofanov et al., 2012) data, and the drill tailings APXS (Campbell et al., 2014; Gellert, 2012, 2013) data, within the context of the sedimentology and compared with terrestrial analogs and geochemical models, to reconstruct a possible history of the AMB. We will present hypotheses for how the subsurface and surface water—its composition and conditions—may have reacted with AMB sediments which led to the observed metal enrichments. We will also speculate on the lake's depth, comparing the geochemical evidence in this paper to that of the interpretations of the AMB sedimentology.

Major, minor, and trace elements were analyzed by ChemCam, including major oxides (Clegg et al., 2017), MnO (Gasda et al., 2021), Cu and Zn (Goetz et al., 2023; Lasue et al., 2016), Li, Rb, Sr (Payré et al., 2017), Cr peak area, and Cl, P, Ba, F detection (Forni et al., 2015) and spectral unmixing (Schröder et al., 2023). These data are compiled in the data set for all targets analyzed for this work (excluding float non-AMB rocks, regolith, and out of focus observations; Gasda, Gasnault, et al., 2024). The supplemental data also includes target classification by member, calculated indices of alteration with corrected values for the AMB, and rock type. ChemCam Long distance Remote Micro Images (LDRMI) cover a range of sols from 3042 to 3774 while in situ data was collected from sol 3545 when *Curiosity* observed the first float block that we can confirm by chemistry and textures come from the AMB (target Saracucus). The rover first arrived at a collection of AMB fragments on Sol 3638 and the first outcrop on Sol 3639.

Table 1
Alpha Particle X-Ray Spectrometer Drill Tailing Composition of the Marker Band With Error and Calculated Indices of Alteration

Sol	3682	3684	3721	3744	3767
Target	Amapari 2	Amapari 1	Encanto	Dinira	Tapo Caparo
SiO_2 (wt.%)	26.80 ± 0.32	26.45 ± 0.32	25.71 ± 0.43	24.94 ± 0.43	37.33 ± 0.43
TiO_2 (wt.%)	0.67 ± 0.03	0.68 ± 0.03	0.75 ± 0.05	0.68 ± 0.05	0.76 ± 0.03
Al_2O_3 (wt.%)	3.90 ± 0.19	4.13 ± 0.10	4.66 ± 0.19	4.46 ± 0.19	6.6 ± 0.19
FeO_T (wt.%)	39.86 ± 0.46	42.62 ± 0.46	47.51 ± 0.52	44.58 ± 0.46	25.33 ± 0.26
MgO (wt.%)	5.15 ± 0.17	4.64 ± 0.17	3.44 ± 0.17	5.64 ± 0.25	7.38 ± 0.17
CaO (wt.%)	5.56 ± 0.07	5.37 ± 0.06	5.84 ± 0.10	5.64 ± 0.11	6.58 ± 0.07
Na_2O (wt.%)	3.32 ± 0.20	2.81 ± 0.14	1.02 ± 0.68	1.19 ± 0.68	1.86 ± 0.14
K_2O (wt.%)	0.32 ± 0.02	0.29 ± 0.01	0.30 ± 0.02	0.23 ± 0.02	0.39 ± 0.01
MnO (wt.%)	1.13 ± 0.04	1.38 ± 0.04	1.25 ± 0.05	1.23 ± 0.07	0.49 ± 0.03
Zn (wt.%)	1.75 ± 0.05	1.69 ± 0.05	1.91 ± 0.06	1.56 ± 0.05	0.3888 ± 0.012
SO_3 (wt.%)	6.48 ± 0.12	5.42 ± 0.10	5.20 ± 0.15	7.22 ± 0.22	11.2 ± 0.15
Cl (wt.%)	3.22 ± 0.06	2.89 ± 0.05	1.10 ± 0.05	0.91 ± 0.06	0.52 ± 0.02
P_2O_5 (wt.%)	0.46 ± 0.05	0.47 ± 0.05	0.49 ± 0.05	0.44 ± 0.07	0.40 ± 0.02
Cr_2O_3 (wt.%)	0.6 ± 0.03	0.55 ± 0.03	0.58 ± 0.04	0.71 ± 0.06	0.68 ± 0.03
Ni (ppm)	497 ± 50	545 ± 40	477 ± 70	1132 ± 115	377 ± 25
Br (ppm)	4369 ± 135	3919 ± 120	959 ± 30	863 ± 40	37 ± 5
Sum	99.71	99.84	99.90	99.63	100.63
CIA[a]	37.41	38.32	38.58	43.79	52.47
MIA_{ox}[b]	67.71	69.54	73.99	70.51	59.96
MIA_{red}[c]	8.21	8.36	8.99	8.71	16.11
IOL[d]	64.26	66.06	69.08	68.40	48.21
Fe/Mn	35.40	31.00	38.15	36.38	51.88

[a]Chemical Index of Alteration; corrected CaO and Na_2O for apatite, sulfate, and halite. [b]Mafic Index of Alteration (MIA) (oxidizing); corrected CaO, Na_2O, MgO for apatite, sulfate, and halite. [c]MIA (reducing); corrected CaO, Na_2O, MgO for apatite, sulfate, and halite. [d]Index of Laterization.

All APXS data is presented in Thompson et al. (2024). For this paper we use APXS drill tailings data for bulk chemistry of the ripple and laminated units of the AMB. Then we use the ChemCam data on the AMB rocks to track fine-scale chemical changes. We also present the data differently than Thompson et al. (2024) by using the available geochemical information to remove the sulfate and halite contribution in the bedrock to calculate the indices of alteration (see Section 2.1) that will aid in the interpretation of the AMB. Chemistry ternary plots were made using the Python application Quick Ternaries (Essunfeld et al., 2025).

3.1. Indices of Alteration

The Chemical Index of Alteration (CIA), the Mafic Index of Alteration (MIA), and the Index of Laterization (IOL) are all proposed methods to use the major element oxide compositions of materials to understand their likely mechanisms of alteration (Babechuk et al., 2014; Nesbitt & Young, 1984). CIA (Equation 1) tracks the loss of the soluble elements Ca, Na, and K, with respect to Al, and is an indicator of open system weathering in relatively circumneutral conditions, producing kaolinite (Nesbitt & Young, 1984).

$$CIA = 100 \times [Al_2O_3/(Al_2O_3 + CaO + Na_2O + K_2O)] \quad (1)$$

MIA (Equations 2 and 3) is preferable for tracking the initial alteration of mafic materials, adding Mg to the mobile phase, and including Fe_2O_{3T} (total iron oxide, expressed as Fe^{3+}) to understand iron's behavior in reducing

(mobile) versus oxidizing (immobile) conditions (Babechuk et al., 2014). The MIA_{ox} formula (Equation 2) assumes Fe is not in the mobile phase—since $Fe^{2+}_{(aq)}$ will oxidize to form Fe^{3+} and precipitate as Fe_2O_3 in oxidizing conditions—whereas the MIA_{red} (Equation 3) assumes Fe is in the mobile phase because in reducing conditions Fe^{2+} would not oxidize and should remain in solution because Fe^{2+} is soluble in most conditions. So, if MIA_{ox} is increasing, it is likely the rock experienced chemical weathering in oxidizing conditions, and if MIA_{red} is increasing, then those rocks are likely to have experience chemical weathering under reducing conditions. Since Fe accumulates in the AMB rocks, one hypothesis is that MIA_{ox} is most relevant to the in situ alteration of AMB (see Section 5). However, we do not know based on the rover data whether Fe^{2+} or Fe^{3+} is present in these rocks.

$$MIA_{ox} = 100 \times [(Al_2O_3 + Fe_2O_{3T})/(Al_2O_3 + Fe_2O_{3T} + MgO + CaO + Na_2O + K_2O)] \quad (2)$$

$$MIA_{red} = 100 \times [Al_2O_3/(Al_2O_3 + Fe_2O_{3T} + MgO + CaO + Na_2O + K_2O)] \quad (3)$$

IOL (Equation 4) is preferred for more advanced stages of weathering and tracks the loss of silica with respect to Al and Fe in circumneutral conditions, where neither Al nor Fe^{3+} are mobile (Babechuk et al., 2014). Note that Babechuk et al. (2014) plot the data for Equation 3 on a ternary diagram much the same as Nesbitt and Young (1984), but the former assumes all the iron is Fe^{3+} and the latter assumes all the iron is Fe^{2+}. In this paper, we will plot data on the A-CNK-FM diagram assuming iron is Fe^{2+} for easier comparison to past work on Earth and Mars (e.g., Hurowitz et al., 2006).

$$IOL = 100 \times [(Al_2O_3 + Fe_2O_{3T})/(SiO_2 + Al_2O_3 + Fe_2O_{3T})] \quad (4)$$

CIA and MIA all use the molar proportions of the oxides, whereas IOL uses mass (wt.%). In all cases, an index equal to 100 indicates the highest level of weathering and values <40 indicate unweathered basalt (Babechuk et al., 2014).

To determine the CIA, MIA, and IOL, we must first correct the oxides to remove influence from the chemical precipitates in the rock to help interpret indices of alteration. In APXS data, Na_2O, MgO, and CaO have been corrected for sulfate, halite, and apatite using APXS values for S, P, and Cl (on a molar basis), as detailed below. It is not possible to correct the FeO_T values to account for siderite in the laminated unit using ChemCam or APXS data because neither instrument can quantify the carbonate composition of the rocks. Therefore, the FeO_T composition of the silicate fraction of these rocks is likely overestimated by a few wt.%; lowering the FeO_T values will lower the MIA_{ox} and IOL values or increase MIA_{red}.

In ChemCam data, veins or high CaO targets (>20 wt.% CaO targets with high sulfur content) were screened out so we are only considering primarily rock (i.e., non-vein) data before correcting for salts and apatite on a molar basis. There is a nearly 1:1 correlation between Na and Cl in these materials in APXS data, so we could consider halite or perchlorate as possible carriers of excess Na. Both NaCl and $NaClO_4$ have the same molar proportions of Na and Cl (1:1), any method of removing excess Na with Cl should not be affected by the presence or absence of perchlorate, but the presence of perchlorate in this system cannot be entirely ruled out. Other salts would be very minor components, if present (borates and nitrates likely only exist at the ppm level in these rocks). We could not correct for halite using the APXS value for Cl because there are more moles of Cl reported by APXS in the drill tailings than moles Na in the rock estimated by ChemCam. If we assume that Na_2O values that are 3σ above the mean of 2.37 wt.% Na_2O in ChemCam data can all be accounted for by excess Cl, we could reduce the Na_2O in these targets to the average. This only affects one observation point, point 1 in the target Tracaja, in the laminated unit. By reducing the Na_2O value for this target from 10.28 to 2.37 wt.%, its CIA value changes from 29.5 to 50. Due to the variability of Na_2O in other targets, it is hard to assess how much Na could be accounted for by halite in these rocks. Na_2O values for APXS (mean tailings after corrections equal 0.53 wt.% Na_2O) are much lower than that of ChemCam (mean = 2.41 wt.% Na_2O). The ~2 wt.% Na_2O difference between ChemCam and APXS data suggests an up to ~15% relative bias to the CIA value for ChemCam points, and the APXS value suggests that ChemCam CIA values are too low. These corrections affect MIA values less than the CIA values (MIA_{ox} bias ~6.5 relative percent and MIA_{red} bias is ~10 relative percent, both in the positive direction) because of the addition of MgO and Fe_2O_{3T} in those calculations. Na_2O likely should not be reduced to zero because Na-plagioclase is likely present in these rocks based on drill samples collected and below the AMB (e.g., Chipera et al., 2023; Tutolo et al., 2025).

To correct for sulfate in the ChemCam data set, generally MgO or CaO dominates over the other oxide, and we subtract out all the excess CaO or MgO from the rock based on the sulfur predicted by the preliminary sulfur calibration model (Clegg et al., 2020). The SO_3 predicted by the preliminary sulfur calibration model for the drill targets is within ∼1 wt.% of those reported by APXS on the drill tailings. We assume 0.3 wt.% S is intrinsic to the rock, as has been done previously for Mars CIA estimates by Schieber et al. (2017). In a few ChemCam observations, there is a mixture of sulfates (the molar composition of sulfur estimated for the point exceeds the molar amount of CaO or MgO alone). This affects four observation points. We took the molar proportion of MgO versus CaO and corrected the amount of the oxide using the given sulfur composition based on this proportion. This method is also used to correct for two outliers that have very high CIA values in the laminated unit. As a sanity check, the average CaO for the data set is ∼4 wt.% and MgO is ∼3 wt.%, both have a standard deviation of ∼2 wt.%. After correcting these oxides based on their proportion, these four anomalous observations were brought in line with the average and standard deviation of the other data points. APXS and ChemCam values for MgO and CaO are in reasonable agreement after the corrections are made (corrected MgO ripple average composition: 2.8 wt.% for ChemCam vs. 3.2 wt.% for APXS; corrected CaO ripple average composition: 3.6 wt.% for ChemCam vs. 3.2 wt.% for APXS). The small amounts of leftover MgO and CaO are consistent with our assumption that a portion of the rock is pyroxene and plagioclase (i.e., Chipera et al., 2023; Tutolo et al., 2025).

3.2. Dynamic Albedo of Neutrons Analysis

We utilized a series of active neutron measurements taken by the DAN instrument while the *Curiosity* rover was stationed over the AMB on Sols 3645–3715. These measurements were acquired to evaluate the subsurface hydration, reported as water-equivalent hydrogen (WEH), and the macroscopic neutron absorption cross-section (Σ_{eff}), along with their spatial distribution up to a depth of approximately 50 cm at the study site.

$$\sum_{\text{eff}} = \sum_{i}^{N} \sum_{\text{eff},i} = N_A \sum_{i}^{N} \frac{a_i \sigma_{\text{abs},i}}{m_{a,i}} \tag{5}$$

where N_A is Avogadro's number, a_i is the abundance of the ith element in weight fraction, $m_{a,i}$ is the molar mass of the ith element, and $\sigma_{\text{abs},i}$ is the effective microscopic neutron absorption cross-section of the ith element. Σ_{eff} serves as an indicator for the presence of the individual elements that have a high capacity for neutron absorption (denoted as σ_{abs}). On Mars, the elements most frequently associated with high σ_{abs} values include Fe and Cl, though other metals such as Mn, Zn, or Ni can also affect neutron die-away measurements (Hardgrove et al., 2011).

The retrieval of subsurface parameters (WEH and Σ_{eff}) from DAN active data follows the methods described in Gabriel et al. (2018 supplement). However, here we expand the simulation space to include independent variations of both WEH and Σ_{eff} within two subsurface layers to model their variability with depth. Neutron transport from the DAN pulsed-neutron generator (PNG) to the surface, the interactions of neutrons with elements within the subsurface and the detection of neutrons between PNG pulses is simulated using Monte Carlo N-Particle 6, developed by Los Alamos National Laboratory (McKinney et al., 2006; Pelowitz, 2005). The DAN active thermal neutron data (die-away curves) are background subtracted and both simulations and data are normalized. The shapes of the die-away curves are then compared to determine the range of possible subsurface parameters using a Markov Chain Monte Carlo (MCMC) method (Czarnecki et al., 2020; Gabriel et al., 2018). Markov Chain Monte Carlo sampling is used to retrieve posterior probability distributions for WEH content and neutron absorption cross-section (Σ_{eff}). Retrievals are performed for both homogeneous and two-layer subsurface models, with the latter incorporating a boundary depth parameter to account for stratigraphic variability. The posterior distributions obtained from the MCMC analysis provide a quantitative assessment of parameter uncertainties and correlations, which are essential for evaluating subsurface composition and hydration trends. Markov Chain Monte Carlo corner plots, illustrating the relationships among retrieved parameters, are presented in Text S2 in Supporting Information S1.

3.3. Exploratory Geochemical Models

The Geochemist's Workbench (GWB) version 17.0.3 (Bethke et al., 2023) *Phase2* module was used to explore the geochemical controls on metal ion mobility and deposition in the investigated strata. Unlike more commonly

presented activity diagrams (created within GWB using the Act2 module), which only show the most thermodynamically stable phase as a function of the modeler-chosen *x*- and *y*-axes, *Phase2* simulates the chemical evolution of waters by systematically speciating solutions as a function of the covarying *x*- and *y*-axis variables. In this instance, the behavior of a system containing 0.5 mmol/kg NaCl, 1 mmolal S, and 1 mmolal each of Fe, Mn, and Zn, and a fixed CO_2 fugacity of 0.1 bars was speciated as a function of oxygen fugacity ($f_{O_2(g)}$) and pH at 25°C to determine the equilibrium concentrations of these elements. Note that fugacity is approximately equal to pressure, in bars, over the range of pressures considered here. Values of $f_{O_2(g)}$ were chosen to represent the range of O_2 and H_2 partial pressures thought to represent the ancient Martian atmosphere (Wordsworth et al., 2021), from $f_{O_2(g)}$ from 10^{-70} to 0.2 bar, or log $f_{H_2(g)}$ from −41.65 to −6.55. We convert between equilibrium values of log $f_{O_2(g)}$ and $f_{H_2(g)}$ using the following relationship:

$$\log f_{O_2(g)} = -\log K - 2 \log f_{H_2(g)}$$

where log K is the equilibrium constant for the reaction. $2H_{2(g)} + O_{2(g)} = 2\,H_2O$ and is equal to 83.1 at 25°C. For a further discussion of the relative importance of f_{O_2} versus f_{H_2}, we direct the reader to the interesting paper by Hao et al. (2019). While the simulations are fully coupled (i.e., the equilibrium state of the Fe, Mn, and Zn-bearing system is being speciated as a function of the *x*- and *y*-axes), the resultant elemental concentrations and equilibrium phases were output and plotted according to the individual elemental system for clarity. The utility of the *Phase2* approach is that it enables calculation and visualization of elemental concentrations as a function of the chosen independent variables, which are limited at the upper end by the chosen input parameters (e.g., the 1 mmolal S Fe, Mn, and Zn we used to initialize the simulation) or by the solubility of relevant minerals (e.g., Fe, Mn, or Zn-bearing minerals). While either goethite or hematite can precipitate from fluids at the temperatures realistic for Mars, hematite is the most thermodynamically favorable phase, and its solubility only marginally differs from that of goethite. Since we used a temperature of 25°C for all models, and goethite more typically forms at lower temperatures, we only allow goethite to represent Fe (oxyhydr)oxides in these calculations.

4. Results

ChemCam and APXS data agree that the AMB ripple unit has a greatly elevated FeO_T and MnO compared to rock both below and above the AMB (Tables 1 and 2; Gasda, Gasnault, et al., 2024; Gellert, 2012; Thompson et al., 2024). Both data sets also agree that the chemistry of the thickly laminated unit is closer to the average Mars crust. Sulfate increases upsection in the thickly laminated unit, especially near the Tapo Caparo drill target (Tables 1 and 2; Gasda, Gasnault, et al., 2024; Gellert, 2012; Thompson et al., 2024). The second crossing ChemCam data showed high FeO_T and MnO, and Zn was detected, consistent with the first crossing and APXS results. ChemCam data on the AMB ripple unit targets show a strong Fe-Mn correlation (Figure 3a). ChemCam does not detect P in the AMB. MnO has no correlation with S, Cr, nor TiO_2 in ChemCam data. ChemCam only observed Zn and Cu in targets where those elements are above the detection limit for the instrument, and while these enrichments are notable, no conclusive trends with these elements can be determined because most of these detections are below the quantification limit of the current Zn and Cu compositional models (Text S3 in Supporting Information S1). ChemCam observed that nodules all have low MnO (Figure 3c), and Zn was detected in a few of these targets while FeO_T is variable in ChemCam data. In ChemCam data, FeO_T has no correlation with TiO_2 (Figure 4a), is anticorrelated with S and Cr (Figures 4b and 4c). The exception is the Curucuquero nodule target which has a positive Fe-Ti and Fe-Cr trend, and Zn was detected in two observation points.

Mastcam multispectral observations were taken at the drill locations after cleaning by the dust removal tool but before drilling. ChemCam passive spectra were acquired after drilling on the drill tailings piles. These drill tailings are primarily sourced from inside the rock. The pre-drill Mastcam multispectral spectra are very similar to the ChemCam passive spectra of the drill tailings (Figures 4d and 4e). ChemCam passive spectral data shows minor variations in 535 nm band depth (the least for Encanto and strongest for Amapari). A potential mineralogy match for these spectra is chamosite (see Section 5; Figure 4f) and other potential phases are provided for comparison (Figure 4f, Figure S1 in Supporting Information S1). A more detailed spectral matching of Mastcam multispectral spectra of the AMB with library spectra is provided in Farrand et al. (2025).

Table 2
ChemCam Mean Compositions of the Marker Band Materials With 1σ Standard Deviation and Calculated Indices of Alteration

	Ripples	Nodules	Laminated
N[a]	200	21	66
SiO_2 (wt.%)	40.39 ± 2.78	41.44 ± 5.28	43.23 ± 3.17
TiO_2 (wt.%)	0.71 ± 0.04	0.82 ± 0.25	0.70 ± 0.06
Al_2O_3 (wt.%)	8.11 ± 1.0	8.53 ± 1.66	9.02 ± 1.07
FeO_T (wt.%)	27.41 ± 5.15	24.30 ± 4.37	18.85 ± 1.78
MgO (wt.%)	4.42 ± 1.88	6.18 ± 1.81	8.43 ± 2.88
CaO (wt.%)	5.88 ± 2.19	5.02 ± 2.51	7.14 ± 2.63
Na_2O (wt.%)	2.45 ± 0.58	2.52 ± 0.54	2.09 ± 1.07
K_2O (wt.%)	0.31 ± 0.13	0.53 ± 0.39	0.45 ± 0.14
MnO (wt.%)	1.09 ± 1.33	0.16 ± 0.06	0.22 ± 0.05
SO_3 (wt.%)	6.86 ± 2.57	6.77 ± 2.47	9.78 ± 3.69
Li (ppm)[b]	15.30 ± 3.93	13.55 ± 6.62	10.03 ± 2.85
Cr peak Area ($\times 10^{-5}$)	7.75 ± 2.76	11.83 ± 7.49	11.00 ± 2.48
Sum	97.96	96.40	100.01
CIA	43.79	42.00	38.82
MIA_{ox}	60.85	55.36	47.37
MIA_{red}	17.91	18.16	19.04
IOL	48.68	46.25	40.94
Fe/Mn	68.1	173.6	87.8

[a]Number of ChemCam observations included in mean and standard deviation. [b]Includes non-detections as 0 values.

4.1. Indices of Alteration

Oxidative indices of alteration (MIA_{ox} and IOL) are high while reductive (MIA_{red}) and CIA and are low in the ripple unit drill targets (Tables 1 and 2; Gellert, 2012; Gasda, Gasnault, et al., 2024; Thompson et al., 2024). All the indices of alteration are low in the laminated unit targets (Tables 1 and 2; Gasda, Gasnault, et al., 2024; Gellert, 2012; Thompson et al., 2024). The ripple unit targets span a range of CIA of ~35–60 and up to 55 for the nodules (Figure 5d). Compared to bulk silicate Mars (red down triangle; Taylor, 2013), the CIA of most AMB targets is higher (Figure 5d). MIA_{ox} is higher than bulk silicate Mars as well, and mainly driven by the loss of MgO (Figures 5a and 5c). Compared to the median ChemCam Mount Sharp Group Lacustrine rock composition (Dehouck et al., 2022; Frydenvang et al., 2020), CIA of the AMB is low (Figure 5d), but the AMB has higher MIA_{ox} and IOL than other lacustrine materials in the crater (Figures 5a–5c). For MIA_{ox} and IOL, MnO increases with increasing alteration in the ripple unit (Figures 5a–5c). The nodules in the laminated unit follow these trends, but without the corresponding MnO-enrichment (Figure 3c). The thickly laminated Tapo Caparo drill sample again stands out distinct from the other drill targets. Tapo Caparo's higher CIA is close to that of the median Mount Sharp group lacustrine composition (Figure 5d) and has a lower MIA and IOL than ripple unit targets; Tables 1 and 2, suggesting a different style of alteration in this target.

4.2. Hydration of the AMB

DAN active measurements acquired on Sols 3645 and 3672 indicate that the AMB rippled unit is approximately 100% more hydrated (7.2 ± 2.0 wt.% WEH) than the traverse average (3.6 ± 1.1 wt.% WEH), assuming a homogeneous subsurface (Figure 6). When compared to models of a layered subsurface, the DAN active data at AMB are consistent with an upper layer hydration of 4–8 wt.% WEH within the AMB ripple unit at the Amapari drill site (Figure 6, Text S2, Figure S2 and S3 in Supporting Information S1). This hydration level is lower than that of the Contigo member, which is consistent with the identification of hydrated sulfate minerals in the Canaima drill sample (Chipera et al., 2023), but higher than the Catrimani member with its decreasing sulfate contents just below the AMB (Thompson et al., 2024; Figure 6).

The DAN active data at this location also support the presence of a 35 ± 11 cm thick upper layer, consistent with the thickness of the ripple unit (Figure 1c), and indicate a higher-than-average neutron absorption cross section ($\Sigma_{eff} = 0.02 \pm 0.0022$ cm^2/g). This elevated Σ_{eff} is consistent with the high metal and chlorine content measured by APXS at the first AMB crossing, and Cl is a particularly strong neutron absorber.

A similar water content and layer thickness, but a slightly lower neutron absorption cross section, were observed in the ripple unit near the second crossing (Figure 6, Text S2, Figure S4 and S5 in Supporting Information S1). This decrease in Σ_{eff} is consistent with the drop in Cl concentrations observed at the Encanto and Dinira drill locations compared to Amapari. As the rover traversed through the second crossing, DAN-derived hydration levels decreased to the mean Gale hydration (3.6 ± 2.3 wt.% WEH), and the neutron absorption cross section also declined to the mean Gale value (Figure 6).

4.3. Exploratory Geochemical Models

Geochemical simulations indicate that elevated, millimolal-level concentrations of Fe, Mn, and Zn are only possible under a distinct subset of redox and pH conditions. Of these, Fe solubility is the most restrictive. Our calculations indicate that elevated concentrations of Fe can only be achieved at relatively reducing (by a reducing agent such as H_2 or by the lack of an oxidant, see Section 5.2.4) and acidic conditions—beginning at pH ~6.2 at the lowest investigated f_{O_2} and decreasing to pH < 1.8 at the most oxidizing conditions, with pyrite solubility

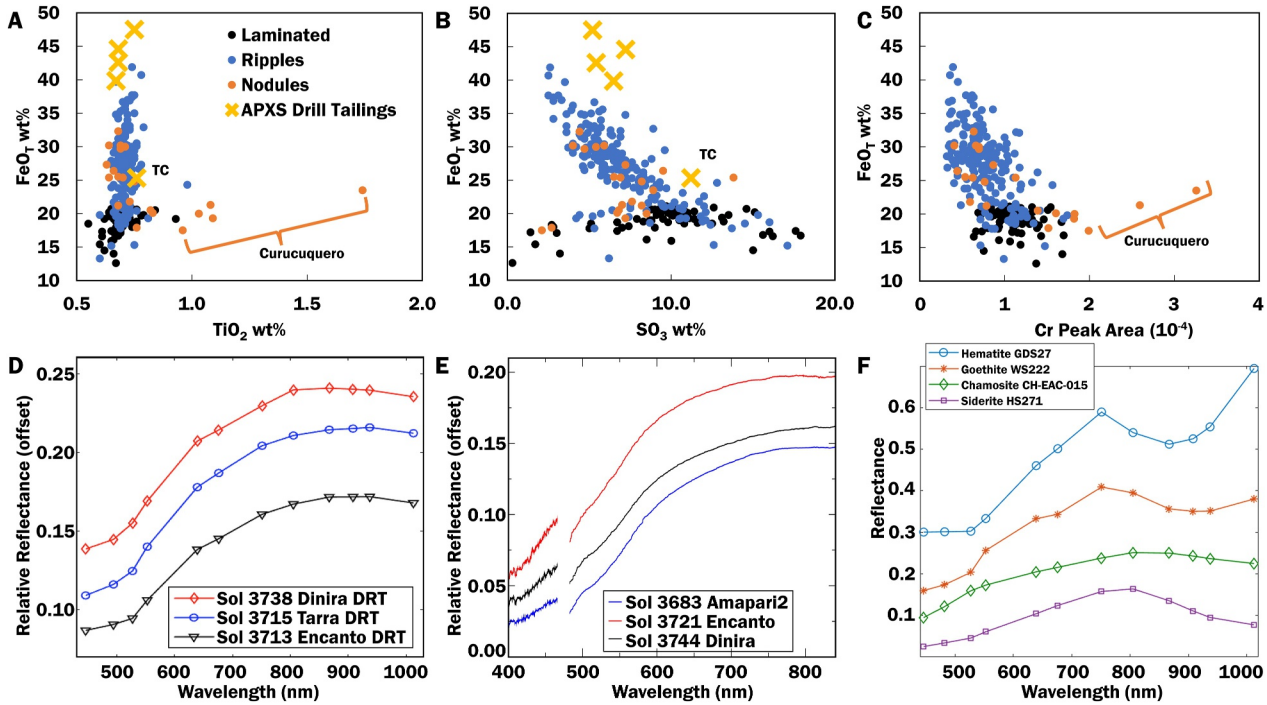

Figure 4. Chemistry and Passive spectra of the Amapari "Marker Band" (AMB) (dots are ChemCam data, Xs are Alpha Particle X-Ray Spectrometer [APXS] data). (a) FeO_T vs. TiO_2. (b) FeO_T vs. SO_3. (c) FeO_T versus Cr peak area (APXS not shown because these cannot be plotted on the same axes, See Table 1). (d) Mastcam multispectral data of Marker Band drill locations. (e) ChemCam passive spectra of Marker Band drill tailings smoothed with a 51-channel filter. (f) RELAB spectra for four Fe-bearing mineral samples that may occur in the AMB. The four spectra are offset for clarity (Hematite—offset up by 0.2757; Goethite—offset up by 0.13; Chamosite—offset down by 0.052; Siderite–offset down by 0.02).

limiting Fe concentrations under a subset of conditions (Figures 7a and 7d). Mn solubility demonstrates the same general behavior, although the relevant Mn oxide (pyrolusite) remains soluble to much more oxidizing conditions (Figures 7b and 7e). Finally, over the calculated range, Zn is the most soluble over the broadest range. Zn remains soluble at pH < 6.5, at $\log(f_{O_{2(g)}}) > \sim -65$, while smithsonite ($ZnCO_3$) controls Zn solubility at higher pH and sphalerite (ZnS) limits its solubility at more reducing conditions, although at the most acidic and reducing of the investigated conditions, neither mineral limits Zn solubility (Figure 7c).

Figure 7 points (i–iv) illustrate different scenarios of fluid conditions. At point (i), pH 5 and reducing conditions ($\log(f_{O_2}) = -60$), Fe, Mn, and Zn are all stable in solution. From point (i), either increasing oxidation, pH, or both, will promote phase precipitation (these diagrams do not convey rates of formation or solid solutions, only pure equilibrium phases). Increasing both pH and oxidation (Figure 7 i–iv) will favor Mn and Fe (oxyhydr)oxides (pyrolusite, hematite, and/or goethite), and zincite or smithsonite to form. The Zn phases will depend on whether CO_2 is present or not. Only increasing oxidation (i–iii) will favor Mn and Fe (oxyhydr)oxides to form, but no Zn phases are stable. When CO_2 is included in the model and increasing pH (Figure 7a–7c i–ii), Zn and Mn carbonate (smithsonite and rhodochrosite, respectively) are more favored for precipitation along with Fe (oxyhydr)oxides, but only in cases where all metals are equally concentrated ($\log(\text{Mn(molal)}) > -6$). If Mn is relatively dilute compared to the other metals and CO_2 is present, then Mn will remain in solution while Fe (oxyhydr)oxides and smithsonite would be favored to form. Increasing pH only without CO_2 (Figure 7d–7f i–ii) will favor Fe (oxyhydr)oxides and zincite to form, but no Mn phases are stable (Figure 7d–7f).

5. Discussion

5.1. Chemistry

The AMB is hydrated, has increased levels of alteration compared to bulk silicate Mars, and the ripple unit especially is more altered and oxidized than the median Mount Sharp group lacustrine bedrock composition (Figures 5 and 6, Table 2). Both the ripple and laminated units fall on trend lines that move away from the CaO,

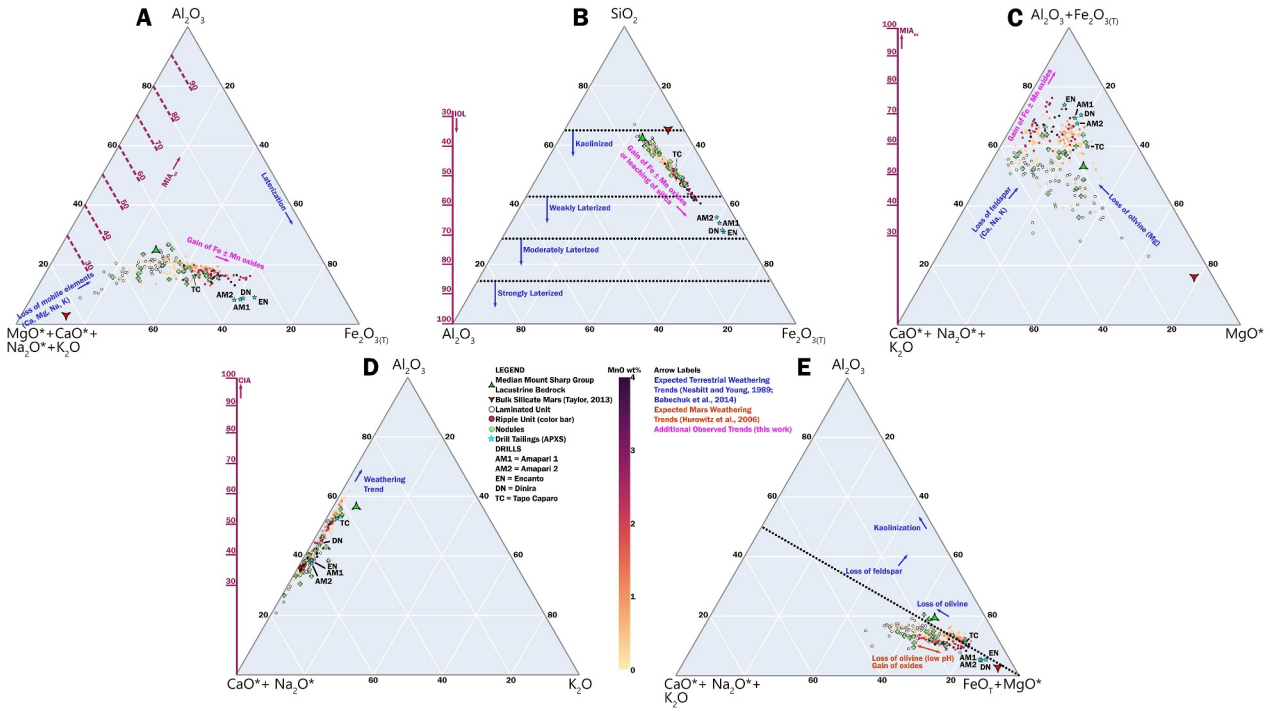

Figure 5. Ternary plots of ChemCam and Alpha Particle X-Ray Spectrometer drill tailings Marker Band bedrock and nodule data that have been corrected for apatite, halite, and sulfate (see Section 3) compared to bulk silicate Mars (Taylor, 2013) and the median Mount Sharp group Lacustrine bedrock ChemCam composition. Ripple layers use the color scale to represent the amount of MnO in wt.% in each observation point. Plots are labeled with appropriate index of alteration (after Babechuk et al., 2014). Trends are labeled blue if expected for terrestrial weathering (Nesbitt & Young, 1984), reddish for Mars weathering at low pH (Hurowitz et al., 2006), or magenta if an additional trend is observed for this work. (a) Molar Al_2O_3-MgO + CaO + Na_2O + K_2O-$Fe_2O_{3(T)}$ ternary diagram with MIA_{ox} plotted. (b) Mass SiO_2-Al_2O_3-$Fe_2O_{3(T)}$ ternary diagram with IOL plotted. (c) Molar Al_2O_3 + $Fe_2O_{3(T)}$-CaO + Na_2O + MgO ternary diagram with MIA_{ox} plotted. (d) Molar Al_2O_3-CaO + Na_2O-K_2O ternary diagram with CIA plotted. (e) Molar Al_2O_3-CaO + Na_2O + K_2O-FeO_T + MgO ternary diagram.

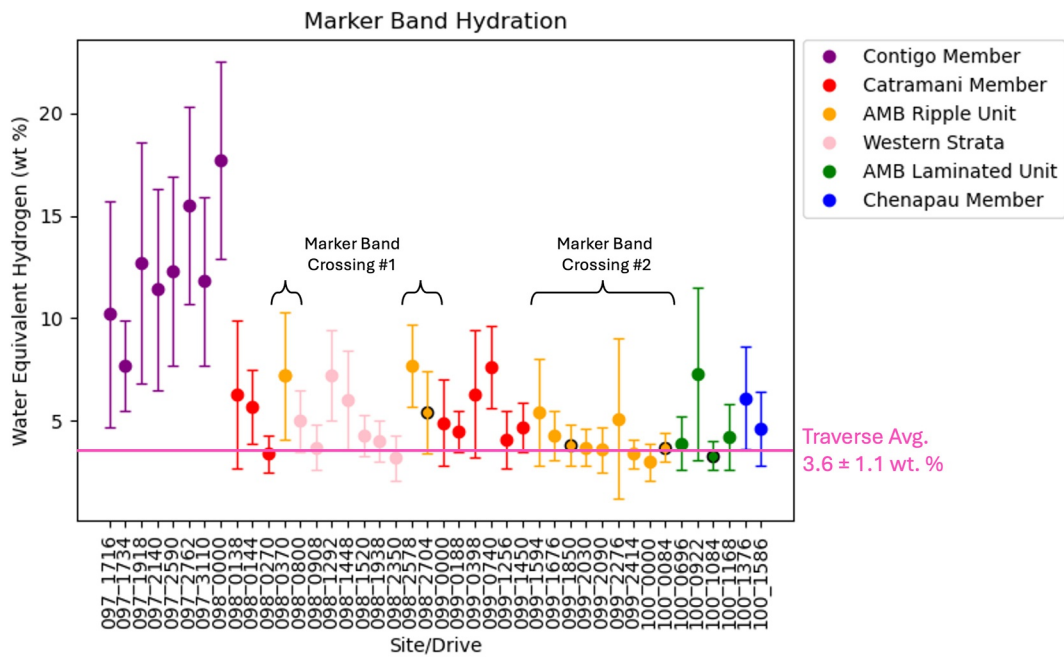

Figure 6. Results from DAN instrument at each rover stop compared to traverse average values (magenta line). Drill sample sites labeled with black outline.

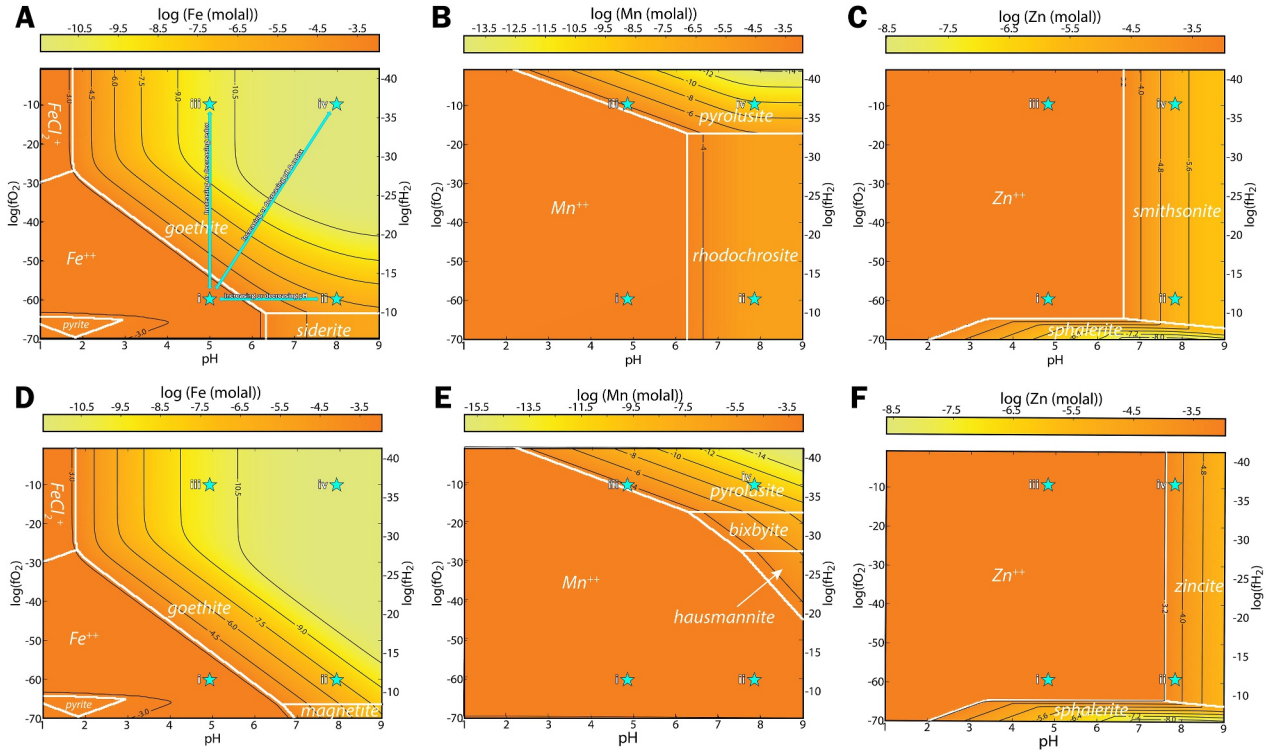

Figure 7. Calculations of Fe, Mn, and Zn solubility as a function of oxygen fugacity ($f_{O_{2(g)}}$) and pH in a Mars-relevant system containing 1 mmolal Fe, Mn, Zn, and S, 0.5 mmol/kg NaCl, and a fixed partial pressure of CO_2 (0.1 bar; a–c) or no inorganic carbon (d–f). Mineral and aqueous ion stability fields are overlain in white, to indicate the limiting factor on the element's concentration. Black lines indicate stability fields for lower concentrations, labeled in log units. Hydrogen fugacity ($fH_{2(g)}$) corresponding to the plotted $f_{O_{2(g)}}$ are indicated along the right *y*-axis. The four cyan stars are in the same location of each diagram: (i) a set of conditions where Fe^{2+}, Mn^{2+}, and Zn^{2+} are soluble in water (pH = 5, $\log(f_{O_2}) = -60$); (ii) a set of conditions where Fe and Zn concentrations are limited by goethite, smithsonite or zincite, and the solubility of Mn is only limited by rhodochrosite when log(Mn (molal)) > −4 and CO_2 is present (pH = 8, $\log(f_{O_2}) = -60$); (iii) a set of conditions where the concentrations of Fe and Mn in solution are limited by the solubilities of goethite and pyrolusite, but Zn is not limited by any mineral solubility (pH = 5, $\log(f_{O_2}) = -10$); (iv) a set of conditions where the concentrations of Fe, Mn, and Zn in solution are limited by the solubilities of goethite, pyrolusite, and smithsonite or zincite (pH = 8, $\log(f_{O_2}) = -10$). Labeled arrows in 7A indicate condition changes either emanating from or approaching star (i).

Na_2O, K_2O, and MgO apices of the ternary diagrams. The laminated unit mainly falls on the trend between bulk silicate Mars and median Mount Sharp group lacustrine bedrock (Figures 5a and 5c), which is consistent with an expected loss of mobile elements, primarily MgO, during aqueous alteration. The ripple unit targets are further oxidized compared to laminated unit targets (Figure 5a–5c) that in Earth settings would correspond to materials that have experienced a greater loss of the mobile elements, but also could correspond to loss of silica and/or gain of Fe and Mn (oxyhydr)oxides (Figures 5a–5c). The nodules fall in between the two units in terms of chemistry. The nodules experienced some weathering along with the loss of silica and/or gain of iron (oxyhydr)oxides, but they lack the gain of Mn (oxyhydr)oxides (Figures 3c and 5b). Thus, it is likely the ripple and laminated units experienced different styles of alteration.

Based on the expected trends for basaltic alteration on Mars and Earth (Babechuk et al., 2014; Hurowitz et al., 2006; Nesbitt & Young, 1984), the locations of the AMB data points in Figure 5a–5c would suggest that most of the rocks in the AMB experienced at least some weathering where Al_2O_3 was mobile (either very low or very high pH conditions, Hurowitz et al., 2006). However, mass balance models based on APXS data suggest that Al_2O_3 was not significantly depleted in the ripple unit (Thompson et al., 2024). Most of the materials experienced loss of MgO (olivine), but not CaO + Na_2O + K_2O (feldspar; Figure 5e). The ripples and nodules are consistent with oxidizing conditions (Figure 5a) as well as laterization (Figure 5b). The higher IOL can be explained either by Fe addition or Si removal. In the latter case, the absolute laterization would suggest kaolin formation or weakly laterized rocks, as expected for terrestrial laterites where kaolinite forms, but in Al-mobile situations, this will not be the case (Figure 5e; see Section 5.2.2). Trends in the APXS data suggest no significant loss or gain of Si or Al, implying Fe addition (Thompson et al., 2024).

Compositionally, the wave ripple laminated material is unique compared to what has been studied in Gale crater. The AMB sediments and nodules have much more FeO_T content compared to previous targets with ripples (e.g., the Prow, lower in the sulfate strata; Caravaca et al., 2025; Gupta et al., 2023), MnO-rich nodules (e.g., Groken in the Glen Torridon phyllosilicate-bearing unit far below AMB; Gasda et al., 2022; Treiman et al., 2023; VanBommel et al., 2023), and MnO-rich sandstones (Gasda, Lanza et al., 2024). Generally, high MnO materials are rare in Gale crater, and thus far the highest MnO contents besides the rippled unit of the AMB, have been the nodules at Groken (Gasda et al., 2022; Treiman et al., 2023). Also, in contrast to Groken, phosphorus is not correlated with Mn-rich targets of the AMB (e.g., Treiman et al., 2023). Previously encountered diagenetic materials have had high FeO_T or MnO content (David et al., 2020; Gasda et al., 2022; L'Haridon et al., 2018, 2020). However, the previously encountered metal-rich mineral-filled fractures (veins) have major differences in metal content (i.e., higher Mn and Ni, no Cu; Gasda et al., 2022) and the Fe oxides were small crystals embedded in calcium sulfate veins with low MnO (David et al., 2020; L'Haridon et al., 2018, 2020). High Zn has been reported previously in lower Mount Sharp and Bradbury Formation rocks and diagenetic veins, sometimes associated with high MnO or other veins (Berger et al., 2017; Lasue et al., 2016). These different fluid compositions imply changing metal transport processes and/or conditions throughout Gale's history. Mn, for example, has a low abundance in Gale materials and compared to crustal rocks in general (Berger et al., 2022; Taylor, 2013). Other locations in Gale where elevated MnO was observed (Sutton Island, Groken) are also consistent with shallow water (Gasda, Lanza et al., 2024; Treiman et al., 2023).

Based on the APXS data, the metal content is decoupled from the salt content of the rocks; FeO_T and MnO remain high in the ripple unit regardless of its Cl and Br content (Table 1; Gellert, 2012; Thompson et al., 2024). This implies a difference in process for the concentration of the more soluble Br and Cl ions versus less-soluble Fe and Mn ions. If we suppose that the first crossing was a regional low point based on the current topography of the AMB over the 300 m mapped (Dietrich et al., 2023), lake water may have accumulated at this position to concentrate ions such as Cl and Br in evaporites. Likewise, Na_2O content is elevated in the Amapari drill tailings, but not the Encanto or Dinira drill tailings (Table 1; Gellert, 2012; Thompson et al., 2024), suggestive of a potential halite contribution to the AMB rocks. However, we do not observe the variation predicted by this hypothesis in other very soluble ions. For example, Li content remained the same (~15 ppm; Gasda, Gasnault, et al., 2024) in the sedimentary rocks at each crossing within the ripple unit.

5.2. Formation Scenarios

Based on the chemical trends, morphological aspects, and passive spectra, three plausible formation hypotheses emerge: (a) concretion formation in shallow water via redox processes, (b) leaching of the sediments in a laterite-like mechanism, (c) diagenetic addition of metal oxides and/or carbonates in an ironstone-like mechanism. Of these three hypotheses, the third is most favored.

The materials in the AMB fall on a chemical trend that suggest a basaltic starting material, followed by a moderately altered laminated unit, and a more altered and oxidized ripple unit. With the assumption of a basaltic starting material, we can explore different scenarios for how the ripple unit could become enriched in Fe, Mn, and Zn, and the nodular section could become Fe- and Zn-rich, but Mn-poor. We rely on minor and trace metals, Ti, Ni, Cu, Cr, and Pb, to understand which of these scenarios are most likely. In addition, we will investigate if the nodules or concretions formed, for example, in multiple groundwater diagenetic episodes, as reworked grains in deeper water, or as a detrital deposit. It is important to note that all the possible formation scenarios have inconsistencies between the observations of similar Earth analogs and that of the AMB. This may be related to the greater effect of biology on Earth. In many cases, alteration and formation of concretions and the depth of redox boundaries in lake sediments are in part controlled by life on Earth (e.g., Brune et al., 2000; Siehl & Thein, 1989; Tebo et al., 2004). More work will be needed (experimental and modeling) to understand the abiotic versus biotic processes that may have led to the AMB formation.

In many cases on Earth, iron-rich materials form in basaltic weathering profiles, including ferromagnesian nodules/concretions, ironstones, laterites, and bauxites (e.g., Siehl & Thein, 1989). Many of these situations occur in wet-dry cycling and oxidizing environments, on Earth's surface in regions that have heavy rainfall, near the top of a stable water table, or in shallow water lakes and seas (e.g., Siehl & Thein, 1989). These environments tend to concentrate Fe, Al, and other trace elements depending on host/source rock composition, groundwater conditions, Eh and pH conditions, and microbial activity (e.g., Siehl & Thein, 1989). Notably, ironstones can preserve fine-

scale textures such as ripple bedforms (Matheson & Pufahl, 2021), but not exclusively. In many cases, Fe-coated grains, mottles, nodules, and concretions form, which can be morphologically similar to the nodules observed at the AMB.

We are not considering banded iron formations or MnO deposits related to the Great Oxygenation Event on Earth as these both tend to have very low Zn content and are likely not good morphologic/genetic analogs to the AMB (e.g., Mücke, 2003; Tsikos & Moore, 1997). Another unlikely formation scenario is stratiform or stratabound hypogene nonsulfide zinc deposits where large sulfide deposits are altered and bring Zn and other chalcophile bearing fluids via faults and fractures to be deposited between stratigraphic layers (Boni & Mondillo, 2015; Hitzman et al., 2003). While these deposits can form nodular materials with high Fe, Mn, and Zn compositions, these deposits tend to have Pb content up to the few percent level (e.g., Coppola et al., 2009; Kyle et al., 2018). APXS did not report elevated Pb or other chalcophiles such as Cu (Thompson et al., 2024), nor do the passive reflectance spectra provide a good match for typical nonsulfide deposit minerals such as willemite or franklinite (Figure S1 in Supporting Information S1).

5.2.1. Crusts, Nodules, and Concretions

In Gale crater, there are many instances where Fe- or Mn-rich fluids have produced early- and late-stage diagenetic features with variable trace element chemistry that point to changing conditions and multiple alteration events (Berger et al., 2022; David et al., 2020; Gasda et al., 2022; Gasda, Lanza et al., 2024; Goetz et al., 2023; Lanza et al., 2016; Rampe et al., 2020; Sun et al., 2019; Thompson et al., 2020, 2024; Thorpe et al., 2022; Treiman et al., 2023; VanBommel et al., 2019, 2022). These include nodular features in Murray and Carolyn Shoemaker formations (Gasda et al., 2022; Sun et al., 2019), Mn-and Fe-rich veins in the Kimberley member of the Bradbury group (Lanza et al., 2016) and in the Carolyn Shoemaker formations (Gasda et al., 2022), Fe- and Mn-rich clasts in Murray formation sulfate veins (David et al., 2020; L'Haridon et al., 2020). Early diagenetic groundwater has also deposited Mn and Fe in sediments in the Murray and Carolyn Shoemaker formations (Gasda et al., 2022; Gasda, Lanza et al., 2024; Goetz et al., 2023), sometimes forming nodules (Gasda et al., 2022; Sun et al., 2019; Treiman et al., 2023). Thus, it appears there was pervasive groundwater that transported Fe and Mn in the Gale crater subsurface, that occasionally interacted at redox fronts to produce various diagenetic features, and that the degree of oxidation, relative concentration of the metals, and kinetics, controlled the amounts of Mn and Fe observed (Figure 7).

On Earth, many observations of manganese (oxyhydr)oxides show how these species are efficient scavengers of trace metals that are present in the groundwater or surface fluids, such as Cu and Zn, depending on pH, but not to the levels required for the AMB (Balistrieri & Murray, 1982; Bradl, 2004; Harriss & Troup, 1970; Hlawatsch et al., 2002; Marcus et al., 2004; Noda et al., 2019; Swanner & Gasda, 2025). Fe (oxyhydr)oxides also scavenge Cu to a lesser extent than Mn (oxyhydr)oxides and Fe (oxyhydr)oxides can adsorb small amounts on Zn, but are not major scavengers of Zn (Bradl, 2004; Manceau et al., 2000; Noda et al., 2019; Trolard et al., 1995). Micro-X-ray studies have shown the Zn is closely associated with Mn in these nodules via an adsorption mechanism (Marcus et al., 2004). Terrestrial deep ocean ferromagnesian (oxyhydr)oxide nodules can have some of the highest Zn contents, up to ∼2,800 ppm in the Peru Basin in the Pacific Ocean (Kuhn et al., 2017; Von Stackelberg, 1997) and shallow marine ferromagnesian nodules, such as those in the Baltic Sea can have up to ∼1,650 ppm Zn (Suess & Djafari, 1977). Mn Carbonate deposits have up to ∼3,450 ppm Zn (Eder et al., 2018). Fe/Mn ratio is generally anticorrelated with Zn content (Asavin et al., 2010; Boström et al., 1982; Calvert & Piper, 1984; Calvert & Price, 1977; Eder et al., 2018; Kuhn et al., 2017; Marino et al., 2017; Pattan & Banakar, 1993; Takahashi et al., 2007; Von Stackelberg, 1997), except for hydrogenetic nodules, which have low Zn and no correlation with Zn (Marino et al., 2017; Takahashi et al., 2007). Terrestrial lacustrine nodules also only have up to 1,940 ppm Zn and tend to have elevated Zn at low Fe/Mn ratios (Calvert & Price, 1970, 1977; Cook & Felix, 1975; Dean, 1970; Harriss & Troup, 1970; Hayles et al., 2021; Moore et al., 1980; Rossmann & Callender, 1968; Schoettle & Friedman, 1971; Sozanski & Cronan, 1979). Terrestrial examples of FeMn concretion-rich soils with elevated Zn show that Fe/Mn ratio is anticorrelated with Zn (e.g., Latrille et al., 2001; Szymański & Skiba, 2013). None of the marine, lacustrine, or sedimentary concretion examples have high enough Zn to account for what is observed in the AMB, nor is it likely that Fe (oxyhydr)oxides would adsorb Zn if Mn (oxyhydr)oxides are present, so Zn concentration in the AMB by adsorption to Fe (oxyhydr)oxides is very unlikely.

It may still be plausible that a multi-stage alteration process occurred at the AMB that resulted in Fe and Zn rich, but Mn poor nodules. Such a scenario could be the early diagenetic cementing of the ripples with high Fe and Mn precipitating from a fluid at a redox front in the shallow subsurface. In a shallow lake, the redox front's position relative to the lake bottom remains the same as sediment fills the lake. As many terrestrial examples show, redox cycling at this front could have occurred beneath the lake, at the sediment lake bottom interface, or subaerially (Harriss & Troup, 1970; Müller et al., 2002; Schwertmann & Fanning, 1976; Szymański et al., 2014). Thus, if Mars is different from Earth and enough Zn could be adsorbed to account for our observations in the AMB, a second diagenetic episode with reducing groundwater would be required to remove Mn from the concretions. However, experiments where nodules were leached with acid to remove Mn, Zn was also leached (e.g., Koschinsky & Hein, 2003). And while the removal of Mn oxide may lead to the "hollowed out" texture of the concretions, it is unlikely that only the inside of the nodules would be removed in this scenario. For example, Marcus et al. (2004) shows that Zn-rich Fe-Mn nodules form concentric or onion-like layers and the Mn is not confined to only the center of the concretion. Thus, the hypothesis that Zn is concentrated in the AMB via an adsorption mechanism is inconsistent with observations in the AMB and leads us to explore other mechanisms to produce Fe- and Zn-rich nodules without Mn oxide.

5.2.2. Laterites

Based on the chemical trends in the AMB ripple unit, the ripples are more oxidized than the laminated unit, the nodules, and other lacustrine materials in Gale crater, and the ripple unit follows a trend to higher laterization (Figure 5). In this hypothetical scenario, a period of intense weathering ensues that would break down overlying layers and enriches Fe in the underlying ripples. That weathering would continue until the top surface breaks down producing a hard nodular crust that is then buried by new laminated sediment. Many basaltic laterites have a gradient of increasing Fe_2O_{3T} and Zn from bottom to top due to subaerial weathering (Babechuk et al., 2014; Campodonico et al., 2019). Manganese can be enriched in oxidized zones within the laterite (e.g., Ma et al., 2007). Fe-rich concretions form an upper hard crust or as a stone/gravel layer within the sediments (Babechuk et al., 2014; Campodonico et al., 2019), that then may undergo further alteration to remove material much like what we observe in the hollow nodules within the AMB (Swanson, 1923; Tardy & Nahon, 1985). Microanalysis of Fe and Zn in laterized grains show a close association of Zn and Fe in detrital Fe-Ti oxides and Fe-rich veins in the Deccan Traps laterites (Suhr et al., 2018; Supporting Information S1). Of the basalt-derived laterite examples from Earth, the Deccan Traps laterite profile is most similar to that of the AMB, with a lowermost section of the laterite profile with very high Fe_2O_{3T} and low Al_2O_3 and the upper nodular laterite that is Fe_2O_{3T}-rich (Babechuk et al., 2014; Suhr et al., 2018). Argentinian laterites of Serra Geral basalts are somewhat similar levels of IOL, but these are kaolinite-rich with high Fe_2O_{3T} (Fe_2O_{3T} enrichments similar to Al_2O_3, Campodonico et al., 2019). Southern China Hainan Island basalt-derived laterite has experienced extreme levels of weathering (Al_2O_3 enrichments greater than Fe_2O_{3T}, Ma et al., 2007).

However, several lines of evidence rule out laterites as a mechanism to produce the AMB. The same process that would break down the surface to enrich Fe would also likely not preserve the fine-scale ripple textures observed in the AMB. Advanced laterization is ruled out based on low initial Al_2O_3 and mass balance models that suggest Al_2O_3 was not significantly removed during alteration (Thompson et al., 2024). Titanium should be immobile in the moderate levels of laterization implied by chemistry of the AMB, TiO_2 is enriched in terrestrial basaltic laterites, and Zn is commonly a minor element constituent of the refractory FeTi grains (Babechuk et al., 2014; Campodonico et al., 2019; Ma et al., 2007; Suhr et al., 2018). In the AMB, no positive correlation between FeO_T and TiO_2 or between IOL and TiO_2 was observed. Where Fe_2O_{3T} contents are highest in the Deccan Traps profile, Zn is enriched by 2× in bulk from the unaltered basalt (Suhr et al., 2018) and up to 8× in the most resistant (but small) Fe-Ti grains (Suhr et al., 2018; Supporting Information S1). The 2× enrichment in the bulk rock is not enough to explain the enhancement of Zn observed by APXS in the AMB; ∼100× enrichment is required to increase the zinc content observed in Bagnold sands and average basaltic Mars regolith (193 and 293 ppm Zn, respectively; O'Connell-Cooper et al., 2017) to the levels APXS observed in the AMB. Ni is also not enriched in APXS data (Thompson et al., 2024), which is not consistent with laterization trends (e.g., Ma et al., 2007).

5.2.3. Ironstones

In contrast to laterites, ironstones form at the bottom of shallow bodies of water or in the shallow subsurface from upwelling anoxic, sometimes hydrothermal, pore water interacting with a redox front to form Fe-rich cements and

concretions (Di Bella et al., 2019; Matheson & Pufahl, 2021). This process can also form "ooids," which has genetic and biological connotations, thus more recent literature refers to these as Fe-coated grains (Matheson & Pufahl, 2021). The grains can be coated with Fe (oxyhydr)oxides or with chamosite (Fe-bearing chlorite) or its precursors (bertherine or iron silicate gel), depending on the redox environment in which they form (Matheson & Pufahl, 2021). Terrestrial ironstone outcrops have few centimeters thick interbedded layers of cemented/coated grains with sharp redox boundaries, likely controlled by depositional variability, which can preserve sedimentary structures, including ripple textures (Matheson & Pufahl, 2021). Diagenetic alteration of the goethite coated grains can form hematite or siderite to varying degrees depending on the conditions, but chamosite only alters into ferroan carbonate instead of hematite (Matheson & Pufahl, 2021; Mücke, 2006; Mücke & Farshad, 2005). Manganese is not typically enhanced in these types of deposits but can be present in small amounts in siderite, goethite, or as part of the groundmass (Mücke & Farshad, 2005).

Passive reflectance spectra of the AMB drill tailings and dust removed Mastcam target spectra on ripple unit targets are somewhat consistent with chamositic ironstone, but not convincingly so. A lack of peaks in the spectra is not diagnostic of a particular Fe mineral, but chamosite is not inconsistent with the spectra (Figures 4d–4f; Milliken, 2020). The AMB spectra are anomalous compared to other Gale sedimentary rocks in that they do not have a clear hematite or goethite signature as we might expect with the very high FeO_T content of the rocks. However, in the ChemCam passive spectra we would expect to see –OH bands near 700 and 900 nm, but these may not be present in mixtures of chamosite and other minerals (Figure 4). Manganese oxide minerals are dark, and it is characteristic of dark materials to lower the contrast of absorption features (e.g., Clark, 1983).

While on Earth hematite and chamosite will typically coat grains of quartz or carbonates (Matheson & Pufahl, 2021), a recent study has shown goethite coatings around basaltic materials, including plagioclase, pyroxene, and volcanic glass, at an 80 m depth near Panarea, Italy (Di Bella et al., 2019). Hence, ironstone formation may be a pathway to produce FeMn (oxyhydr)oxides or carbonates around basaltic grains in the ripple unit that experienced higher degrees of oxidation in shallow water, and coated grains that are high Fe and Zn without Mn in lakebed nodules. Those nodules could have experienced lower degrees of oxidation in deeper water due to redox stratification as lake levels rose (e.g., Hurowitz et al., 2017).

Geochemically, terrestrial ironstones can be enriched in P, Cr, Ti, and other siderophiles (Garnit & Bouhlel, 2017; Lottermoser & Ashley, 1996; Matheson & Pufahl, 2021; Mücke, 2006; Mücke & Farshad, 2005; Siehl & Thein, 1989), though the geochemistry of the materials will be highly dependent on the primary material that is being coated and the chemistry and conditions of the fluid. Phosphorus could be enriched in ironstones owing to their relationship with marine environments (Matheson & Pufahl, 2021; Siehl & Thein, 1989), thus related to life on Earth, so we cannot deduce whether the lack of P in the AMB would rule out ironstone-style Fe-coated grains at the AMB. And while some Mn-rich concretions in Gale crater have enrichments in P (Treiman et al., 2023), other Mn- and Fe-rich deposits do not (Gasda et al., 2022; Gasda, Lanza et al., 2024). Apart from one nodule target, there is a negative relationship between FeO_T and Cr peak area in ChemCam spectra, and Cr is depleted in the ripple unit and nodules compared to the laminated unit in ChemCam data (Figure 4c). The Cr composition of the two units is within error for the APXS data set. This trend may be consistent with chromium's higher solubility in oxic conditions (e.g., Cole et al., 2018) favored for the ripple unit. There is no correlation between TiO_2 and FeO_T in the AMB rocks within the ChemCam and APXS data sets, except for the Curucuquero target, where there is a positive correlation (Figure 4a). The positive relationship in the Curucuquero target between Ti and Cr suggests detrital input for this target (e.g., Cole et al., 2018).

Given that the fluids that produce ironstones can be hydrothermally sourced, this may also be a pathway for Zn enrichment in these sediments (see Section 5.2.4). In many terrestrial analog examples, ironstones are very low in Zn (Di Bella et al., 2019; Lottermoser & Ashley, 1996) with some that have enrichments up to ∼0.1 wt.% Zn (Garnit & Bouhlel, 2017). However, the highest Zn enrichments are strongly correlated with high Mn (Garnit & Bouhlel, 2017; Salama et al., 2012). These examples are in stark contrast to AMB, where Zn needs to be 10× more enriched than the terrestrial examples, and Zn and Mn are not correlated in the nodular rocks of the AMB.

5.2.4. Comparison of Models

The Ironstone (additive diagenetic model) has advantages over the laterite (leaching model), but the additive model does not fully explain all of the observations. Both models provide plausible mechanisms for Fe and Mn enrichments in the ripple unit, but only the ironstone mechanism provides a way to preserve ripple unit textures.

Passive reflectance data is not conclusive, but the data is overall not consistent with hematite, goethite, or siderite, and somewhat consistent with chamosite coated grains in the ripples. Both scenarios produce hydrated minerals (e.g., phyllosilicates, goethite; Babechuk et al., 2014; Matheson & Pufahl, 2021) that would be consistent with the DAN data of the AMB. Ironstone formation is highly dependent on many factors, including sediment mineralogy and composition, and fluid composition, in some cases involving acidic (pH 2–5) and reducing fluids up to ∼140°C interacting at the lake or seabed sediment water-interface redox zone (e.g., Di Bella et al., 2019). The close association of siderite with ironstones due to redox and pH changes in the environment makes ironstones compelling for the AMB; the Tapo Caparo drill sample within the AMB has the highest amount of siderite ever observed in the crater (∼10%, Tutolo et al., 2025). Certainly, more modeling will be needed using Gale-relevant fluid compositions to understand the source of Zn, its transport fluid conditions, if any, and the phase that hosts Zn.

5.2.5. Potential Sources of Zn in Gale Crater

Groundwater circulation and leaching of Zn across Gale crater sedimentary rocks or in its source region may have been able to produce a reducing fluid that can transport Fe, Mn, and Zn provided that it is S-poor (e.g., Lasue et al., 2016; Figure 7). The surrounding sediments are enriched in Mg sulfate that is very soluble in groundwater. Thus, sulfate content of this fluid is likely to be high. Our preliminary models show that sulfate content restricts the conditions where the metals are fluid mobile (Figure 7). There is no indication that the metal enrichments in the AMB are sulfates; sulfur is low in the AMB, and there is no correlation between S and the metals in the AMB. Instead, our preliminary model favors acidic groundwater conditions, which widens in more dilute groundwater conditions, which passed through a chemical front to produce the observed metal enrichments (Figure 7).

Alteration of primary zinc (sphalerite) enriched sediment is also suggested by Lasue et al. (2016). The temperature of these fluids (up to 200°C; Lasue et al., 2016) is in line with ironstone-forming hydrothermal fluids (Di Bella et al., 2019). However, sphalerite deposits would also likely host other chalcophile sulfides, such as PbS and/or CuS. Trace metal contents of primary martian sulfides are not well-understood, but one study of hydrothermal sulfides in a martian meteorite shows that Pb, Cu, and Zn are present in the sulfides in roughly similar amounts (Lorand et al., 2018). If martian sulfides are the source of Zn for the AMB, the AMB would be a few weight percent enriched in Pb and Cu based on typical terrestrial examples, along with Zn (e.g., Boni & Mondillo, 2015; Hitzman et al., 2003). Pb, Cu, and other chalcophiles are not enriched in the AMB according to APXS results (Thompson et al., 2024), and Cu is only found up to ∼500 ppm in ChemCam data (Figure S7 in Supporting Information S1). Thus, we think a sulfide alteration process is unlikely.

Studies of trace chalcophiles in martian meteorites suggest the main carrier of Zn is in primary FeTi oxides and chromite grains, as well as pyroxenes, but only chromite is not a significant carrier of Cu or Pb (Barrat & Bollinger, 2010; Lorand et al., 2015; Wang et al., 2004). Since chromites and FeTi oxides are refractory, these phases could have provided Zn detritally to the AMB. However, we would expect to observe a correlation between Fe and Ti or Cr in the data, but if this correlation originally existed, it may have been overprinted by Fe oxide addition. Fe and Cr are anticorrelated in ChemCam data and Fe and Ti have no clear correlation in targets in the AMB, besides the Curucuquero target (Figures 4a and 4c). So, if detrital Zn in refractory grains was provided to the AMB, it was either only a minor component or was completely overprinted by later diagenesis. Thus, weathering of basalts may be the only source of Zn in fluids that deposited metals in the AMB. The weathering of basalts may be consistent with the hypothesis of Berger et al. (2017) that suggested the sedimentary source region for Gale crater has been hydrothermally altered to form Zn-rich phases.

While recent calculations indicate that even if solutions that deposited metals in the AMB contained millimolal-level concentrations of Fe, prodigious volumes of water would be needed (Kite et al., 2025), which may be incompatible with a drier martian climate. Our exploratory models indicate that relatively reduced groundwater fluids would have been required to mobilize the Fe, Mn, and Zn observed in the deposit (Figure 7), consistent with early diagenetic models of metal ion mobility in Gale crater (Rampe et al., 2017). Yet, a significant perturbation of redox and/or pH would be required to subsequently deposit these metals. To this end, a relatively reducing, relatively acidic groundwater (any set of fluid conditions where Fe^{2+}, Mn^{2+}, and Zn^{2+} are soluble in solution, and one example condition is labeled by the (i) cyan star in Figure 7) could have scavenged the metals from bedrock, transported the metals to the AMB, and then ultimately deposited them upon exposure to a shallow, standing water body equilibrated with an O_2 and possibly CO_2-rich atmosphere (Figure 8). Oxidants other than O_2 such as

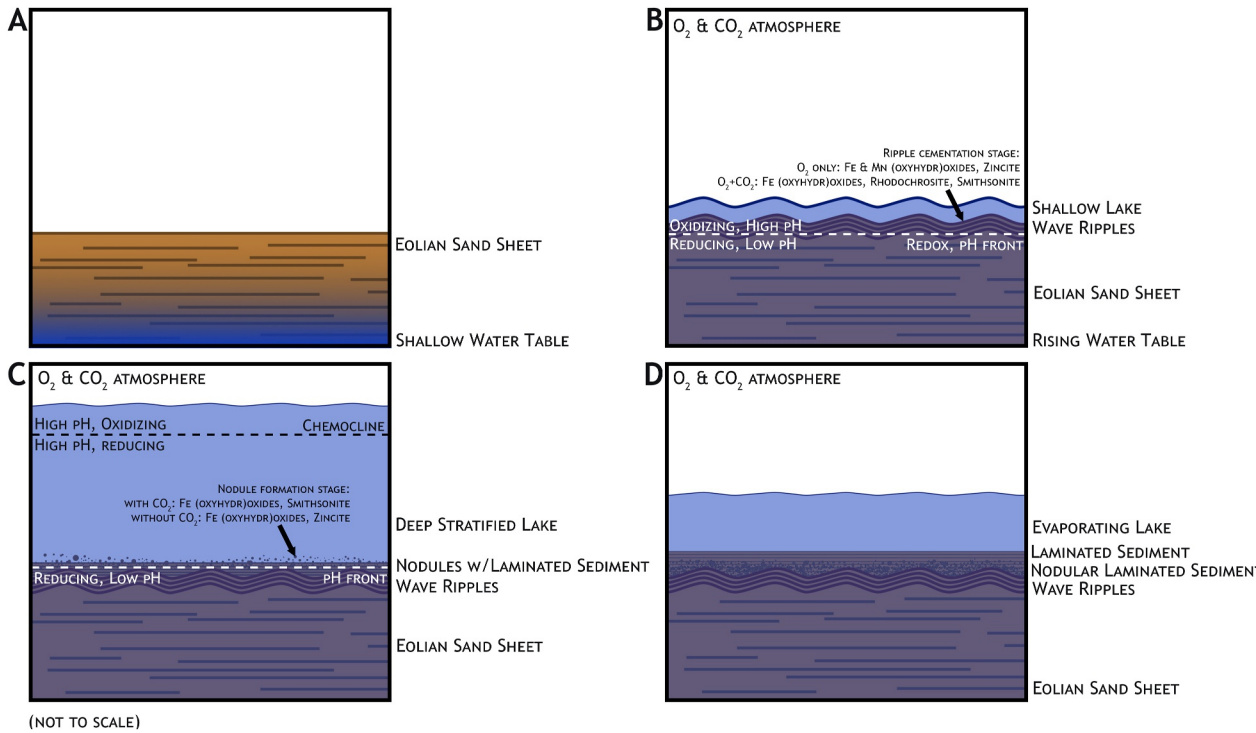

Figure 8. Illustration of a possible mechanism to form metal enrichments in the Amapari "Marker Band" (AMB). (a) A high Fe and Zn concentration, with relatively low Mn concentration, mildly acidic, and reducing shallow groundwater (Figure 7i) in the eolian sandsheet environment below the AMB. (b) This groundwater rises to the surface to form a shallow lake and interacts with an O_2 (or other oxidants) and possibly CO_2-bearing atmosphere. A redox and pH front forms in the shallow subsurface where wave ripple bedforms also form that promotes metal oxide or carbonate precipitation (Figure 7 i–iv). (c) A deeper stratified lake forms that is reducing at its depths and precludes wave ripple bedform formation. The groundwater reacts across a pH front within the layers where nodules form (Figure 7 i–ii). (d) The groundwater begins to retreat below the subsurface as the lake evaporates. The CO_2 in the water could become concentrated in the water to promote siderite formation in the laminated layers of the AMB (i.e., Tutolo et al., 2025).

photochemical oxidants or perchlorates, are unlikely because of the conditions needed to precipitate Mn (oxyhydr)oxides are more constrained than that of Fe (oxyhydr)oxides (Gasda, Lanza, et al., 2024).

5.2.6. Synthesis

A key constraint on these formation scenarios is the presence of ripples that would have formed in a shallow lake, followed by a deeper lake to deposit overlying layers (Mondro, Grotzinger, et al., 2025). The ripple unit would have formed while interacting with the atmosphere in no more than 2.0 m of water; ripples would not form if the lake was covered with ice (Mondro, Fedo, et al., 2025). In fully oxygenated water columns on Earth, oxic-anoxic boundaries can be very sharp with millimeters of thickness in the sediment at the base of the lake, but sometimes much deeper depending on the level of microbial activity (Brune et al., 2000), but here we will only consider abiotic scenarios. A shallow oxygenated lake could promote Mn and Fe oxidation, but not Zn oxide formation (Figure 7 i–ii). If CO_2 is present in the atmosphere, the shallow water is likely to be carbonate rich as well. These more oxidizing and higher pH conditions would promote all three metal oxide and/or carbonate phases to precipitate (Figure 7 i–iv). Lake levels then became deeper to a point of cutting off ripple formation and atmospheric interaction at depth. The oxic-anoxic boundary depth in the water columns is more difficult to constrain, and terrestrial examples vary from a few meters to 100 s of meters in stratified lakes (Mayr et al., 2020). Redox stratified lakes have been proposed for Gale based on observations earlier in the mission (Hurowitz et al., 2017), and here we suggest a lake could be stratified chemically due to CO_2 in addition to redox. Deep stratified lakes may have sharp CO_2 and pH gradients in either an increasing or decreasing relation with depth, and these chemical boundaries can occur at ∼10–100 m depth in terrestrial lakes (e.g., Boehrer & Schultz, 2008). Our preliminary model suggests that to separate Mn from Fe and Zn phases in the presence of CO_2, a brine that is relatively concentrated in Zn and relatively dilute in Mn is needed ($\log(\text{Zn (molal)}) > -5$; $\log(\text{Mn (molal)}) < -6$, respectively; Figure 7); the model is insensitive to the concentration of Fe in the fluid. Since Zn and Fe are

observed in the nodules with low Mn, the fluid needs to pass through a pH transition but remain in reducing conditions and remain relatively Mn- and/or CO_2-poor to prevent Mn phase precipitation (Figure 7 i–ii).

Thus, what began as a very shallow lake became at least 10–100 s of meters deep. The lake could have become stratified and the chemical front could have moved upward from within the sediments into the water column to promote separation of these phases. We favor this diagenetic model, which is similar to the formation of ironstones, and that is consistent with the other observations in this region (e.g., sandsheets; Mondro, Grotzinger, et al., 2025; Roberts et al., 2025; Figure 8). The underlying Catrimani members' stratigraphy is consistent with a rising water table (Mondro, Grotzinger, et al., 2025; Roberts et al., 2025; Figure 8a). This upwelling groundwater formed a shallow lake, where ripple bedforms were produced, and groundwater passed through a chemical front to deposit the metals in the ripple unit (Figure 8b). Then a deeper lake formed where it was no longer possible to form ripple bedforms (Mondro, Fedo, et al., 2025), and laminated strata was deposited instead (Figure 8c). The chemical front within the ripple unit is likely both a redox and pH front based on the geochemical model (Figure 7), where the relatively more acidic and reducing groundwater became more oxidizing while pH increased (Figure 8b). With or without addition of CO_2, these changes led to Fe, Mn, and Zn phase precipitation (Figure 7 i–iv) cementing the ripples. In the deeper redox stratified alkaline lake (Figure 7 i–ii), Mn (oxyhydr) oxides could no longer form, and if Mn concentrations are also low, rhodochrosite also could not form, but upwelling groundwater may continue to coat grains with Fe and Zn-bearing phases. Lastly, this deeper lake would have disappeared, such as by evaporation, concentrating the CO_2 in solution if it was present. Evaporation of the lake is most consistent with the Tutolo et al. (2025) model, where they suggest that CO_2 must become highly concentrated before siderite can precipitate and could likely only occur when the water table is evaporating just below the surface. Thus, implying that while the laminated unit was deposited in a deep lake, that deep lake must have fully disappeared before the siderite was deposited in the layers where Tapo Caparo was sampled by the rover. Furthermore, this model is consistent with a bolide impact hypothesis that suggests brief warming periods occurred early in Mars' history to produce a short-lived O_2 spike in the CO_2 rich atmosphere on early Mars (Wordsworth et al., 2021). The reductant is likely to be H_2 gas which forms as a byproduct of olivine alteration in the deep subsurface (e.g., Sleep et al., 2004), a gas which was also likely key to enabling brief warm and humid periods on ancient Mars (Adams et al., 2025).

6. Conclusions

In summary, the sedimentary rock textures are consistent with a lake that became deeper over time. Eolian material of the sulfate unit was eroded down to a deflation surface (with a gently undulating surface), upon which the AMB was deposited. At first, at least in the location explored by the rover, the lake was shallow enough to form wave ripples. We hypothesize that groundwater bearing Fe, Mn, Zn welled up from a rising water table from the underlying Catrimani member that was likely sulfate bearing, slightly acidic, and reducing. This groundwater rose to the surface and encountered a redox and pH front. First, a shallow lake would have been present, and this lake became oxidized, and CO_2 content may have risen due to interaction with the atmosphere. Then this atmospheric interaction with the shallow lake possibly led to precipitation of Mn (oxyhydr)oxides or carbonate, Fe (oxyhydr)oxides, and Zn oxide or carbonate, which could coat the primary basaltic materials (with a minor Zn-bearing refractory chromite and FeTi grain component) deposited at this location and cement the ripples or form nodules. The shallow lake was then likely followed by a deeper stratified lake and at depth it was less oxidizing, but CO_2 could still present at depth. So, we predict Fe (oxyhydr)oxides and either Zn oxide or carbonate would precipitate without rhodochrosite or MnFe (oxyhydr)oxides due to low Mn content in the water and due to anoxic conditions. These precipitates could form coated grains or nodules on the lake floor.

Some issues remain with the hypothesis presented in this work. More modeling that takes water-to-rock ratios into account will be needed to constrain the concentration of Fe, Mn, and Zn in solution, as well as other ions, the source of the metals to form this deposit and the conditions of their precipitation. We have established that the amount of O_2 that could form in the atmosphere during transient events (possibly driven by impacts) can form Mn (oxyhydr)oxides on Mars. Further climate, atmospheric, and kinetic modeling work is needed to determine whether the length of time required to precipitate the Mn (oxyhydr)oxides is compatible with the possible lifetime of a shallow lake related to warming of Mars during transient events.

A few other, but less likely, scenarios cannot be fully ruled out. Mn and Fe oxides may have initially formed in the ripple unit and then became partially reduced in the presence of CO_2 and anoxic conditions to produce Mn-

bearing siderite due to changing conditions in a deep stratified lake. The thickly laminated unit was deposited on top of the nodules, but this unit experienced a different style of weathering, so a lake may not be necessary to explain the deposition of the laminated unit.

The AMB lake deposit is distinctive in its possible >1,500 km^2 lateral extent, stratigraphic confinement, and thinness. The AMB is a unique feature in Gale crater both in terms of the excellently preserved wave ripple bedforms and metal enrichments. Regardless of the emplacement models, metal enrichments imply some kind of chemical interface, and a large amount of water movement at the surface and subsurface, which was previously unexpected for this time period on Mars. Questions remain regarding the water source and possible climate drivers for lake formation. Likely the AMB was a short episode of water activity in an otherwise drying climate, similar to other aqueous features such as polygonal evaporitic features and ripple bedforms observed lower in the Mirador formation. These episodes of surface aqueous activity point to a continuation of Gale's subsurface aqueous activity, which has important implications for preservation of habitable environments in the martian subsurface.

Redox sensitive elements, including Fe and Mn, can be used by life on Earth as energy sources (Brune et al., 2000; Mayr et al., 2020; Tebo et al., 2004). Chemical fronts within stratified lakes or lake sediments are habitable environments that host thriving microbial communities on Earth (Brune et al., 2000; Gulati & Zadereev, 2017; Mayr et al., 2020; Tebo et al., 2004). Given the exciting astrobiological implications raised by the AMB, these types of materials should be prioritized for future *Curiosity* wet chemistry analysis or for Mars Sample Return from Jezero crater should the opportunity arise.

Acknowledgments
The authors want to provide a special acknowledgment to Horton E. Newsom (1952–2024) for his support and encouragement of this work. He will be greatly missed. The authors thank JPL for building and operating the *Curiosity* rover, as well as the NASA Mars Exploration Program, NASA Mars Science Laboratory Participating Scientist Program, the Canadian Space Agency, and CNES for their support. O. Gasnault acknowledges funding from CNES (grant code 180027). E. Kite acknowledges funding Grant 80NSSC22K0731. S. J. VanBommel acknowledges funding Grant 80NSSC22K0650. J.R. Johnson acknowledges funding Grant 80NSSC22K0779. R. Sheppard acklowledges funding Grant 80NSSC23K0189. W. Goetz acknowledges the support from the Deutsche Forschungsgemeinschaft (DFG, GO 2288/2-1). W. Dietrich acknowledges funding to conduct this work was also in part provided through Malin Space Science Systems. The research was partly carried out at the Jet Propulsion Laboratory, California Institute of Technology, under a contract with the National Aeronautics and Space Administration (80NM0018D0004). J. Frydenvang acknowledges the support from the Carlsberg Foundation. S. P. Schwenzer acknowledges funding from The Research England's grant "Expanding Excellence in England" 124.18 and internal funds from The Open University. The authors thank two anonymous reviewers and Andrew Heard for providing constructive comments that improved the manuscript. Mastcam mosaics were processed by the Mastcam team at Malin Space Science Systems. Any use of trade, firm, or product names is for descriptive purposes only and does not imply endorsement by the U.S. Government.

Conflict of Interest

The authors declare no conflicts of interest relevant to this study.

Availability Statement

All ChemCam spectra (R. Wiens, 2021a, 2021b), RMIs (R. Wiens, 2021c, 2021d), APXS data (Gellert, 2012, 2013), Mastcam images (Malin, 2021a, 2021b), and MAHLI images (Edgett, 2021a, 2021b, 2021c) used in this work are available from the Planetary Data System (PDS) Geoscience Node (https://pds-geosciences.wustl.edu/missions/msl/chemcam.htm) and the PDS Imaging Node (https://pds-imaging.jpl.nasa.gov/data/mahli/ and https://pds-imaging.jpl.nasa.gov/data/mastcam/). CSV files are provided as a separate data set with the chemistry of the individual ChemCam observation points, LDRMIs used for mapping the AMB, and APXS drill tailings data (Gasda, Gasnault, et al., 2024).

References

Achilles, C. N., Rampe, E. B., Downs, R. T., Bristow, T. F., Ming, D. W., Morris, R. V., et al. (2020). Evidence for multiple diagenetic episodes in Ancient fluvial-lacustrine sedimentary rocks in gale crater, Mars. *Journal of Geophysical Research: Planets*, *125*(8), e2019JE006295. https://doi.org/10.1029/2019JE006295

Adams, D., Scheucher, M., Hu, R., Ehlmann, B. L., Thomas, T. B., Wordsworth, R., et al. (2025). Episodic warm climates on early Mars primed by crustal hydration. *Nature Geoscience*, *18*(2), 133–139. https://doi.org/10.1038/s41561-024-01626-8

Allen, P. A. (1997). *Earth surface processes*. Blackwell Science.

Asavin, A. M., Kubrakova, I. V., Mel'nikov, M. E., Tyutyunnik, O. A., & Chesalova, E. I. (2010). Geochemical zoning in ferromanganese crusts of Ita-MaiTai guyot. *Geochemistry International*, *48*(5), 423–445. https://doi.org/10.1134/S0016702910050010

Babechuk, M. G., Widdowson, M., & Kamber, B. S. (2014). Quantifying chemical weathering intensity and trace element release from two contrasting basalt profiles, Deccan Traps, India. *Chemical Geology*, *363*, 56–75. https://doi.org/10.1016/j.chemgeo.2013.10.027

Balistrieri, L. S., & Murray, J. W. (1982). The adsorption of Cu, Pb, Zn, and Cd on goethite from major ion seawater. *Geochimica et Cosmochimica Acta*, *46*(7), 1253–1265. https://doi.org/10.1016/0016-7037(82)90010-2

Banham, S. G., Gupta, S., Rubin, D. M., Watkins, J. A., Sumner, D. Y., Edgett, K. S., et al. (2018). Ancient martian aeolian processes and palaeomorphology reconstructed from the Stimson formation on the lower slope of Aeolis Mons, Gale crater, Mars. *Sedimentology*, *65*(4), 993–1042. https://doi.org/10.1111/sed.12469

Barrat, J.-A., & Bollinger, C. (2010). Geochemistry of the Martian meteorite ALH 84001, revisited: Geochemistry of ALH 84001. *Meteoritics & Planetary Sciences*, *45*(4), 495–512. https://doi.org/10.1111/j.1945-5100.2010.01042.x

Bennett, K. A., Fox, V. K., Bryk, A., Dietrich, W., Fedo, C., Edgar, L., et al. (2023). The curiosity rover's exploration of Glen Torridon, gale crater, Mars: An overview of the campaign and scientific results. *Journal of Geophysical Research: Planets*, *128*(1), e2022JE007185. https://doi.org/10.1029/2022JE007185

Berger, J. A., King, P. L., Gellert, R., Clark, B. C., Flood, V. A., McCraig, M. A., et al. (2022). Manganese mobility in gale crater, Mars: Leached bedrock and localized enrichments. *Journal of Geophysical Research: Planets*, *127*(10), e2021JE007171. https://doi.org/10.1029/2021JE007171

Berger, J. A., Schmidt, M. E., Gellert, R., Boyd, N. I., Desouza, E. D., Flemming, R. L., et al. (2017). Zinc and germanium in the sedimentary rocks of Gale Crater on Mars indicate hydrothermal enrichment followed by diagenetic fractionation. *Journal of Geophysical Research: Planets*, *122*(8), 1747–1772. https://doi.org/10.1002/2017JE005290

Berger, J. A., VanBommel, S. J., Rampe, E. B., Knight, A. L., Ustunisik, G. K., & Righter, K. (2024). Copper, Gallium, Zinc, and germanium in Gale crater soils: New constraints on the global enrichment of volatile elements on the martian surface. In *Presented at the 55th lunar and planetary science conference, the woodlands, TX, abstract 1584*.

Bethke, C. M., Farrell, B., & Sharifi, M. (2023). The geochemist's workbench® release 17.

Bibring, J.-P., Langevin, Y., Mustard, J. F., Poulet, F., Arvidson, R., Gendrin, A., et al. (2006). Global mineralogical and aqueous Mars history derived from OMEGA/Mars Express data. *Science*, *312*(5772), 400–404. https://doi.org/10.1126/science.1122659

Boehrer, B., & Schultz, M. (2008). Stratification of Lakes. *Reviews of Geophysics*, *46*(2). https://doi.org/10.1029/2006RG000210

Boersma. (1970). *Distinguishing features of wave ripple cross-stratification and morphology, Thesis*. Utrecht University.

Boni, M., & Mondillo, N. (2015). The "Calamines" and the "Others": The great family of supergene nonsulfide zinc ores. *Ore Geology Reviews*, *67*, 208–233. https://doi.org/10.1016/j.oregeorev.2014.10.025

Boström, K., Wiborg, L., & Ingri, J. (1982). Geochemistry and origin of ferromanganese concretions in the Gulf of Bothnia. *Marine Geology*, *50*(1–2), 1–24. https://doi.org/10.1016/0025-3227(82)90058-5

Bradl, H. B. (2004). Adsorption of heavy metal ions on soils and soils constituents. *Journal of Colloid and Interface Science*, *277*(1), 1–18. https://doi.org/10.1016/j.jcis.2004.04.005

Brune, A., Frenzel, P., & Cypionka, H. (2000). Life at the oxic–anoxic interface: Microbial activities and adaptations. *FEMS Microbiology Reviews*, *24*(5), 691–710. https://doi.org/10.1016/s0168-6445(00)00054-1

Calvert, S. E., & Piper, D. Z. (1984). Geochemistry of ferromanganese nodules from DOMES site a, Northern Equatorial Pacific: Multiple diagenetic metal sources in the deep sea. *Geochimica et Cosmochimica Acta*, *48*(10), 1913–1928. https://doi.org/10.1016/0016-7037(84)90374-0

Calvert, S. E., & Price, N. B. (1970). Composition of manganese nodules and manganese carbonates from Loch Fyne, Scotland. *Contributions to Mineralogy and Petrology*, *29*(3), 215–233. https://doi.org/10.1007/BF00373306

Calvert, S. E., & Price, N. B. (1977). Chapter 3 shallow water, Continental Margin and lacustrine nodules: Distribution and geochemistry. In *Elsevier oceanography series* (Vol. 15, pp. 45–86). Elsevier. https://doi.org/10.1016/S0422-9894(08)71017-1

Campbell, J. L., King, P. L., Burkemper, L., Berger, J. A., Gellert, R., Boyd, N. I., et al. (2014). The Mars Science Laboratory APXS calibration target: Comparison of Martian measurements with the terrestrial calibration. *Nuclear Instruments and Methods in Physics Research Section B: Beam Interactions with Materials and Atoms*, *323*, 49–58. https://doi.org/10.1016/j.nimb.2014.01.011

Campodonico, V. A., Pasquini, A. I., Lecomte, K. L., García, M. G., & Depetris, P. J. (2019). Chemical weathering in subtropical basalt-derived laterites: A mass balance interpretation (Misiones, NE Argentina). *Catena*, *173*, 352–366. https://doi.org/10.1016/j.catena.2018.10.027

Caravaca, G., Gupta, S., Rapin, W., Schieber, J., Le Deit, L., Mangold, N., et al. (2025). Prow & Co.: Inside the fluvial lenses of Gale's layered sulfate unit. In *Presented at the 2025 Lunar and Planetary Science Conference, the Woodlands, TX, abstract 1389*.

Chipera, S. J., Vaniman, D. T., Rampe, E. B., Bristow, T. F., Martínez, G., Tu, V. M., et al. (2023). Mineralogical investigation of mg-sulfate at the Canaima drill site, gale crater, Mars. *Journal of Geophysical Research: Planets*, *128*(11), e2023JE008041. https://doi.org/10.1029/2023JE008041

Clark, R. N. (1983). Spectral properties of mixtures of montmorillonite and dark carbon grains: Implications for remote sensing minerals containing chemically and physically adsorbed water. *Journal of Geophysical Research*, *88*(B12), 10635–10644. https://doi.org/10.1029/jb088ib12p10635

Clegg, S. M., Frydenvang, J., Anderson, R. B., Vaniman, D. T., Gasda, P., Forni, O., et al. (2020). Quantitative Sulfur chemistry observed on diverse samples from sols 1800–2300. In *Presented at the 51st lunar and planetary science conference, the woodlands, TX, abstract 2561*.

Clegg, S. M., Wiens, R. C., Anderson, R., Forni, O., Frydenvang, J., Lasue, J., et al. (2017). Recalibration of the Mars Science Laboratory ChemCam instrument with an expanded geochemical database. *Spectrochimica Acta Part B: Atomic Spectroscopy*, *129*, 64–85. https://doi.org/10.1016/j.sab.2016.12.003

Cole, D. B., O'Connell, B., & Planavsky, N. J. (2018). Authigenic chromium enrichments in Proterozoic ironstones. *Sedimentary Geology*, *372*, 25–43. https://doi.org/10.1016/j.sedgeo.2018.05.002

Cook, D. O., & Felix, D. W. (1975). Ferromanganese deposits in the saranac Lake System New York. *Journal of Great Lakes Research*, *1*(1), 10–17. https://doi.org/10.1016/S0380-1330(75)72332-8

Coppola, V., Boni, M., Gilg, H. A., & Strzelska-Smakowska, B. (2009). Nonsulfide zinc deposits in the Silesia–Cracow district, Southern Poland. *Mineralium Deposita*, *44*(5), 559–580. https://doi.org/10.1007/s00126-008-0220-4

Czarnecki, S., Hardgrove, C., Gasda, P. J., Gabriel, T. S. J., Starr, M., Rice, M. S., et al. (2020). Identification and description of a silicic volcaniclastic layer in Gale crater, Mars, using active neutron interrogation. *Journal of Geophysical Research: Planets*, *125*(3), e2019JE006180. https://doi.org/10.1029/2019JE006180

David, G., Cousin, A., Forni, O., Meslin, P.-Y., Dehouck, E., Mangold, N., et al. (2020). Analyses of high-iron sedimentary bedrock and diagenetic features observed with ChemCam at vera Rubin Ridge, gale crater, Mars: Calibration and characterization. *Journal of Geophysical Research: Planets*, *125*(10), e2019JE006314. https://doi.org/10.1029/2019JE006314

Dean, W. E. (1970). Fe-Mn oxidate crusts in Oneida Lake, New York. In *Proceedings of the 13th conference on Great Lakes research* (pp. 217–226). International Association for Great Lakes Research.

Dehouck, E., Cousin, A., Mangold, N., Frydenvang, J., Gasnault, O., Forni, O., et al. (2022). Bedrock geochemistry and alteration history of the clay-bearing Glen Torridon region of Gale crater, Mars. *Journal of Geophysical Research: Planets*, *127*(12), e2021JE007103. https://doi.org/10.1029/2021JE007103

Di Bella, M., Sabatino, G., Quartieri, S., Ferretti, A., Cavalazzi, B., Barbieri, R., et al. (2019). Modern iron ooids of hydrothermal origin as a proxy for Ancient deposits. *Scientific Reports*, *9*(1), 7107. https://doi.org/10.1038/s41598-019-43181-y

Dietrich, W. E., Bryk, A. B., Kite, E. S., Lewis, K. W., Gupta, S., Weitz, C. M., et al. (2023). Implications of the local topography of the marker band contact, gale crater. In *Presented at the 54th lunar and planetary science conference, the woodlands, TX abstract 1421*.

Eder, V. G., Föllmi, K. B., Zanin, Y. N., & Zamirailova, A. G. (2018). Manganese carbonates in the Upper Jurassic Georgiev Formation of the Western Siberian marine basin. *Sedimentary Geology*, *363*, 221–234. https://doi.org/10.1016/j.sedgeo.2017.11.012

Edgar, L. A., Fedo, C. M., Gupta, S., Banham, S. G., Fraeman, A. A., Grotzinger, J. P., et al. (2020). A lacustrine paleoenvironment recorded at vera Rubin Ridge, gale crater: Overview of the sedimentology and stratigraphy observed by the Mars science laboratory curiosity rover. *Journal of Geophysical Research: Planets*, *125*(3), e2019JE006307. https://doi.org/10.1029/2019JE006307

Edgett, K. S. (2021a). MSL Mars Hand Lens Imager 2 EDR image V1.0 [Dataset]. *NASA Planetary Data System*. https://doi.org/10.17189/1520187

Edgett, K. S. (2021b). MSL Mars Hand Lens Imager 2 EDR ZSTACK V1.0 [Dataset]. *NASA Planetary Data System*. https://doi.org/10.17189/1520396

Edgett, K. S. (2021c). MSL Mars Hand Lens Imager 4 RDR ZSTACK V1.0 [Dataset]. *NASA Planetary Data System*. https://doi.org/10.17189/1520169

Edgett, K. S., Caplinger, M. A., Maki, J. N., Ravine, M. A., Tony Ghaemi, F., McNair, S., et al. (2015). Curiosity's robotic arm-mounted Mars Hand Lens Imager (MAHLI): Characterization and calibration status. https://doi.org/10.13140/RG.2.1.3798.5447

Essunfeld, A., Morris, R. A., Comellas, J. M., Gasda, P. J., Lanza, N. L., Clegg, S., et al. (2025). Quick ternaries: Open-source geochemical data visualization software. In *Mars presented at the 56th lunar and planetary science conference, the woodlands, TX abstract 2033*.

Farrand, W. H., Eng, A. M., Trussell, A. R., Johnson, J. R., Bell, J. F., III, Banham, S. G., et al. (2025). Multispectral properties of rocks in Marker Band Valley and evidence for an alteration unit below the Amapari Marker Band at Gale Crater, Mars. *Journal of Geophysical Research: Planets*, *130*(4), e2024JE008645. https://doi.org/10.1029/2024JE008645

Forni, O., Gaft, M., Toplis, M. J., Clegg, S. M., Maurice, S., Wiens, R. C., et al. (2015). First detection of fluorine on Mars: Implications for Gale Crater's geochemistry: First detection of fluorine on Mars. *Geophysical Research Letters*, *42*(4), 1020–1028. https://doi.org/10.1002/2014GL062742

Fraeman, A. A., Edgar, L. A., Rampe, E. B., Thompson, L. M., Frydenvang, J., Fedo, C. M., et al. (2020). Evidence for a diagenetic origin of vera Rubin Ridge, Gale Crater, Mars: Summary and synthesis of curiosity's exploration campaign. *Journal of Geophysical Research: Planets*, *125*(12), e2020JE006527. https://doi.org/10.1029/2020JE006527

Frydenvang, J., Mangold, N., Wiens, R. C., Fraeman, A. A., Edgar, L. A., Fedo, C., et al. (2020). The chemostratigraphy of the Murray formation and role of diagenesis at Vera Rubin ridge in Gale crater, Mars, as observed by the ChemCam instrument. *Journal of Geophysical Research: Planets*, *125*(9), e2019JE006320. https://doi.org/10.1029/2019JE006320

Gabasova, L. R., & Kite, E. S. (2018). Compaction and sedimentary basin analysis on Mars. *Planetary and Space Science*, *152*, 86–106. https://doi.org/10.1016/j.pss.2017.12.021

Gabriel, T. S., Hardgrove, C., Czarnecki, S., Rampe, E., Rapin, W., Achilles, C., et al. (2018). Water abundance of dunes in gale crater, mars from active neutron experiments and implications for amorphous phases. *Geophysical Research Letters*, *45*(23), 12–766. https://doi.org/10.1029/2018gl079045

Garnit, H., & Bouhlel, S. (2017). Petrography, mineralogy and geochemistry of the Late Eocene oolitic ironstones of the Jebel Ank, Southern Tunisian Atlas. *Ore Geology Reviews*, *84*, 134–153. https://doi.org/10.1016/j.oregeorev.2016.12.026

Gasda, P., Gasnault, O., Goetz, W., Schröder, S., & Das, D. (2024). Dataset for the manuscript "Amapari Marker Band Metal-Enrichments: Potential Mechanisms and Implications for Surface and Subsurface Water and Weathering in Gale crater" [Dataset]. *Zenodo*. https://doi.org/10.5281/ZENODO.11137057

Gasda, P. J., Anderson, R. B., Cousin, A., Forni, O., Clegg, S. M., Ollila, A., et al. (2021). Quantification of manganese for ChemCam Mars and laboratory spectra using a multivariate model. *Spectrochimica Acta Part B: Atomic Spectroscopy*, *181*, 106223. https://doi.org/10.1016/j.sab.2021.106223

Gasda, P. J., Comellas, J., Essunfeld, A., Das, D., Bryk, A. B., Dehouck, E., et al. (2022). Overview of the morphology and chemistry of diagenetic features in the Clay-Rich Glen Torridon unit of Gale crater, Mars. *Journal of Geophysical Research: Planets*, *127*(12), e2021JE007097. https://doi.org/10.1029/2021JE007097

Gasda, P. J., Lanza, N. L., Meslin, P.-Y., Lamm, S. N., Cousin, A., Anderson, R., et al. (2024). Manganese-rich sandstones as an indicator of ancient oxic lake water conditions in Gale crater, Mars. *Journal of Geophysical Research: Planets*, *129*(5), e2023JE007923. https://doi.org/10.1029/2023JE007923

Gellert, R. (2012). MSL APXS calibrated bundle. https://doi.org/10.17189/RRMC-DG75

Gellert, R. (2013). MSL Mars alpha particle X-Ray spectrometer 4/5 RDR V1.0. https://doi.org/10.17189/1518757

Goetz, W., Dehouck, E., Gasda, P. J., Johnson, J. R., Meslin, P., Lanza, N. L., et al. (2023). Detection of copper by the ChemCam instrument along curiosity's traverse in gale crater, Mars: Elevated abundances in Glen Torridon. *Journal of Geophysical Research: Planets*, *128*(3), e2021JE007101. https://doi.org/10.1029/2021JE007101

Grotzinger, J. P., Crisp, J., Vasavada, A. R., Anderson, R. C., Baker, C. J., Barry, R., et al. (2012). Mars science laboratory Mission and science investigation. *Space Science Reviews*, *170*(1–4), 5–56. https://doi.org/10.1007/s11214-012-9892-2

Grotzinger, J. P., Gupta, S., Malin, M. C., Rubin, D. M., Schieber, J., Siebach, K., et al. (2015). Deposition, exhumation, and paleoclimate of an ancient lake deposit, Gale crater, Mars. *Science*, *350*(6257), aac7575. https://doi.org/10.1126/science.aac7575

Grotzinger, J. P., Sumner, D. Y., Kah, L. C., Stack, K., Gupta, S., Edgar, L., et al. (2014). A habitable fluvio-lacustrine environment at Yellowknife Bay, gale crater, Mars. *Science*, *343*(6169), 1242777. https://doi.org/10.1126/science.1242777

Gulati, R., & Zadereev, E. (2017). Conclusion: Ecology of meromictic Lakes (pp. 379–398). https://doi.org/10.1007/978-3-319-49143-1_13

Gupta, S., Dietrich, W. E., Lewis, K. W., Kite, E. S., Mondro, C., Schieber, J., et al. (2023). 'High' but not So dry on aeolis mons: Transient Lake systems in Hesperian deserts in Gale crater. In *Presented at the 54th lunar and planetary science conference, the woodlands, TX abstract 2707*.

Hao, J., Sverjensky, D. A., & Hazen, R. M. (2019). Redox states of Archean surficial environments: The importance of H_2,g instead of O_2,g for weathering reactions. *Chemical Geology*, *521*, 49–58. https://doi.org/10.1016/j.chemgeo.2019.05.022

Hardgrove, C., Moersch, J., & Drake, D. (2011). Effects of geochemical composition on neutron die-away measurements: Implications for Mars Science Laboratory's Dynamic Albedo of Neutrons experiment. *Nuclear Instruments and Methods in Physics Research Section A: Accelerators, Spectrometers, Detectors and Associated Equipment*, *659*(1), 442–455. https://doi.org/10.1016/j.nima.2011.08.058

Harriss, R. C., & Troup, A. G. (1970). Chemistry and origin of freshwater ferromanganese concretions: Freshwater ferromanganese concretions. *Limnology & Oceanography*, *15*(5), 702–712. https://doi.org/10.4319/lo.1970.15.5.0702

Hayles, S., Al, T., Cornett, J., Harrison, A., & Zhao, J. (2021). Growth rates for freshwater ferromanganese concretions indicate regional climate change in eastern Canada at the Northgrippian-Meghalayan boundary. *The Holocene*, *31*(8), 1250–1263. https://doi.org/10.1177/09596836211011652

Hitzman, M. W., Renolds, N. A., Sangster, D. F., Allan, C. R., & Carmam, C. E. (2003). Classification, Genesis, and exploration guides for nonsulfide zinc deposits. *Economic Geology*, *98*(4), 685–714. https://doi.org/10.2113/gsecongeo.98.4.685

Hlawatsch, S., Neumann, T., van den Berg, C. M. G., Kersten, M., Harff, J., & Suess, E. (2002). Fast-growing, shallow-water ferro-manganese nodules from the western Baltic Sea: Origin and modes of trace element incorporation. *Marine Geology*, *182*(3–4), 373–387. https://doi.org/10.1016/S0025-3227(01)00244-4

Hurowitz, J. A., Grotzinger, J. P., Fischer, W. W., McLennan, S. M., Milliken, R. E., Stein, N., et al. (2017). Redox stratification of an ancient lake in Gale crater, Mars. *Science*, *356*(6341), eaah6849. https://doi.org/10.1126/science.aah6849

Hurowitz, J. A., McLennan, S. M., Tosca, N. J., Arvidson, R. E., Michalski, J. R., Ming, D. W., et al. (2006). In situ and experimental evidence for acidic weathering of rocks and soils on Mars. *Journal of Geophysical Research*, *111*(E2). https://doi.org/10.1029/2005JE002515

Kite, E. S., Gasda, P., Tino, C. J., Weitz, C., Thompson, L., Tutolo, B. M., et al. (2025). Hypotheses for the water and metal fluxes to the rippled Amapari Marker Band, Gale Crater, Mars. *Earth and Planetary Science Letters*, *660*, 119347. https://doi.org/10.1016/j.epsl.2025.119347

Koschinsky, A., & Hein, J. R. (2003). Uptake of elements from seawater by ferromanganese crusts: Solid-phase associations and seawater speciation. *Marine Geology*, *198*(3–4), 331–351. https://doi.org/10.1016/S0025-3227(03)00122-1

Kronyak, R. E., Kah, L. C., Edgett, K. S., VanBommel, S. J., Thompson, L. M., Wiens, R. C., et al. (2019). Mineral-Filled fractures as indicators of multigenerational fluid flow in the pahrump hills member of the Murray Formation, gale crater, Mars. *Earth and Space Science*, *6*(2), 238–265. https://doi.org/10.1029/2018EA000482

Kuhn, T., Wegorzewski, A., Rühlemann, C., & Vink, A. (2017). Composition, Formation, and occurrence of polymetallic nodules. In R. Sharma (Ed.), *Deep-sea mining* (pp. 23–63). Springer International Publishing. https://doi.org/10.1007/978-3-319-52557-0_2

Kyle, J. R., Ahn, H., & Gilg, H. A. (2018). Nature and origin of the nonsulfide zinc deposits in the Sierra Mojada District, Coahuila, Mexico: Constraints from regional geology, petrography, and isotope analyses. *Mineralium Deposita*, *53*(8), 1095–1116. https://doi.org/10.1007/s00126-018-0797-1

Lanza, N. L., Wiens, R. C., Arvidson, R. E., Clark, B. C., Fischer, W. W., Gellert, R., et al. (2016). Oxidation of manganese in an ancient aquifer, Kimberley formation, Gale crater, Mars: Manganese fracture fills in Gale crater. *Geophysical Research Letters*, *43*(14), 7398–7407. https://doi.org/10.1002/2016GL069109

Lasue, J., Clegg, S. M., Forni, O., Cousin, A., Wiens, R. C., Lanza, N., et al. (2016). Observation of > 5 wt % zinc at the Kimberley outcrop, Gale crater, Mars: ZN detection at Kimberley with CHEMCAM. *Journal of Geophysical Research: Planets*, *121*(3), 338–352. https://doi.org/10.1002/2015JE004946

Latrille, C., Elsass, F., Van Oort, F., & Denaix, L. (2001). Physical speciation of trace metals in Fe–Mn concretions from a rendzic lithosol developed on Sinemurian limestones (France). *Geoderma*, *100*(1–2), 127–146. https://doi.org/10.1016/S0016-7061(00)00083-5

L'Haridon, J., Mangold, N., Fraeman, A. A., Johnson, J. R., Cousin, A., Rapin, W., et al. (2020). Iron mobility during diagenesis at vera Rubin Ridge, gale crater, Mars. *Journal of Geophysical Research: Planets*, *125*(11), e2019JE006299. https://doi.org/10.1029/2019JE006299

L'Haridon, J., Mangold, N., Meslin, P.-Y., Johnson, J. R., Rapin, W., Forni, O., et al. (2018). Chemical variability in mineralized veins observed by ChemCam on the lower slopes of Mount Sharp in Gale crater, Mars. *Icarus*, *311*, 69–86. https://doi.org/10.1016/j.icarus.2018.01.028

Lorand, J.-P., Hewins, R. H., Humayun, M., Remusat, L., Zanda, B., La, C., & Pont, S. (2018). Chalcophile-siderophile element systematics of hydrothermal pyrite from Martian regolith breccia NWA 7533. *Geochimica et Cosmochimica Acta*, *241*, 134–149. https://doi.org/10.1016/j.gca.2018.08.041

Lorand, J.-P., Hewins, R. H., Remusat, L., Zanda, B., Pont, S., Leroux, H., et al. (2015). Nickeliferous pyrite tracks pervasive hydrothermal alteration in Martian regolithbreccia: A study in NWA 7533. *Meteoritics & Planetary Sciences*, *50*(12), 2099–2120. https://doi.org/10.1111/maps.125652099

Lottermoser, B. G., & Ashley, P. M. (1996). Geochemistry and exploration significance of ironstones and barite-rich rocks in the Proterozoic Willyama Supergroup, Olary Block, South Australia. *Journal of Geochemical Exploration*, *57*(1–3), 57–73. https://doi.org/10.1016/S0375-6742(96)00016-7

Ma, J.-L., Wei, G.-J., Xu, Y.-G., Long, W.-G., & Sun, W.-D. (2007). Mobilization and re-distribution of major and trace elements during extreme weathering of basalt in Hainan Island, South China. *Geochimica et Cosmochimica Acta*, *71*(13), 3223–3237. https://doi.org/10.1016/j.gca.2007.03.035

Malin, M. C. (2021a). MSL MARS MAST Camera 2 EDR IMAGE V1.0 [Dataset]. *NASA Planetary Data System*. https://doi.org/10.17189/1520190

Malin, M. C. (2021b). MSL MARS MAST Camera 4 RDR IMAGE V1.0 [Dataset]. *NASA Planetary Data System*. https://doi.org/10.17189/1520328

Malin, M. C., Ravine, M. A., Caplinger, M. A., Tony Ghaemi, F., Schaffner, J. A., Maki, J. N., et al. (2017). The Mars Science Laboratory (MSL) Mast cameras and Descent imager: Investigation and instrument descriptions: MSL Mastcam/MARDI Descriptions. *Earth and Space Science*, *4*(8), 506–539. https://doi.org/10.1002/2016EA000252

Manceau, A., Schlegel, M. L., Musso, M., Sole, V. A., Gauthier, C., Petit, P. E., & Trolard, F. (2000). Crystal chemistry of trace elements in natural and synthetic goethite. *Geochimica et Cosmochimica Acta*, *64*(21), 3643–3661. https://doi.org/10.1016/S0016-7037(00)00427-0

Marcus, M. A., Manceau, A., & Kersten, M. (2004). Mn, Fe, Zn and as speciation in a fast-growing ferromanganese marine nodule. *Geochimica et Cosmochimica Acta*, *68*(14), 3125–3136. https://doi.org/10.1016/j.gca.2004.01.015

Marino, E., González, F. J., Somoza, L., Lunar, R., Ortega, L., Vázquez, J. T., et al. (2017). Strategic and rare elements in Cretaceous-Cenozoic cobalt-rich ferromanganese crusts from seamounts in the Canary Island Seamount Province (northeastern tropical Atlantic). *Ore Geology Reviews*, *87*, 41–61. https://doi.org/10.1016/j.oregeorev.2016.10.005

Martin, P. E., Farley, K. A., Baker, M. B., Malespin, C. A., Schwenzer, S. P., Cohen, B. A., et al. (2017). A two-step K-Ar experiment on Mars: Dating the Diagenetic Formation of Jarosite from Amazonian Groundwaters: A two-step K-Ar experiment on Mars. *Journal of Geophysical Research: Planets*, *122*(12), 2803–2818. https://doi.org/10.1002/2017JE005445

Matheson, E. J., & Pufahl, P. K. (2021). Clinton ironstone revisited and implications for Silurian Earth system evolution. *Earth-Science Reviews*, *215*, 103527. https://doi.org/10.1016/j.earscirev.2021.103527

Maurice, S., Wiens, R. C., Saccoccio, M., Barraclough, B., Gasnault, O., Forni, O., et al. (2012). The ChemCam instrument suite on the Mars Science Laboratory (MSL) Rover: Science objectives and mast unit description. *Space Science Reviews*, *170*(1–4), 95–166. https://doi.org/10.1007/s11214-012-9912-2

Mayr, M. J., Zimmermann, M., Guggenheim, C., Brand, A., & Bürgmann, H. (2020). Niche partitioning of methane-oxidizing bacteria along the oxygen-methane counter gradient of stratified lakes. *The ISME Journal*, *14*(1), 274–287. https://doi.org/10.1038/s41396-019-0515-8

McKinney, G. W., Durkee, J., Hendricks, J., James, M., Pelowitz, D., Waters, L., & Gallmeier, F. (2006). MCNPX overview. In *Proceedings of the 2006 HSSW, FNAL, IL, LA-UR-06-6206*.

Meyer, M. J., Milliken, R. E., Stack, K. M., Edgar, L. A., Rampe, E. B., Turner, M. L., et al. (2025). Geological context and significance of the clay-sulfate transition region in Mount Sharp, Gale crater, Mars: An integrated assessment based on orbiter and rover data. *Geological Society of America Bulletin*, *137*(1–2), 82–115. https://doi.org/10.1130/B37355.1

Milliken, R. (2020). RELAB spectral database [Dataset]. *NASA Planetary Data system*. https://doi.org/10.17189/1519032

Milliken, R. E., Grotzinger, J. P., & Thomson, B. J. (2010). Paleoclimate of Mars as captured by the stratigraphic record in Gale Crater: Stratigraphy of gale crater. *Geophysical Research Letters*, *37*(4). https://doi.org/10.1029/2009GL041870

Mitrofanov, I. G., Litvak, M. L., Varenikov, A. B., Barmakov, Y. N., Behar, A., Bobrovnitsky, Y. I., et al. (2012). Dynamic Albedo of neutrons (DAN) experiment onboard NASA's Mars science laboratory. *Space Science Reviews*, *170*(1–4), 559–582. https://doi.org/10.1007/s11214-012-9924-y

Mondro, C. A., Fedo, C. M., Grotzinger, J. P., Lamb, M. P., Gupta, S., Dietrich, W. E., et al. (2025). Wave ripples formed in ancient, ice-free lakes in Gale crater, Mars. *Science Advances*, *11*(3), eadr0010. https://doi.org/10.1126/sciadv.adr0010

Mondro, C. A., Grotzinger, J., Fedo, C. M., Lamb, M. P., Gupta, S., Dietrich, W. E., et al. (2025). Depositional environment of the Amapari marker band: Rising water levels formed Kilometer-Scale Lake in gale crater, Mars. *Journal of Geophysical Research: Planets*, *130*(3), e2024JE008606. https://doi.org/10.1029/2024JE008606

Moore, W., Dean, W., Krishnaswami, S., & Borole, D. (1980). Growth rates of manganese nodules in Oneida Lake, New York. *Earth and Planetary Science Letters*, *46*(2), 191–200. https://doi.org/10.1016/0012-821X(80)90005-9

Mücke, A. (2003). General and comparative considerations of whole-rock and mineral compositions of Precambrian iron-formations and their implications. *Neues Jahrbuch für Mineralogie - Abhandlungen*, *179*(2), 175–219. https://doi.org/10.1127/0077-7757/2003/0179-0175

Mücke, A. (2006). Chamosite, siderite and the environmental conditions of their formation in chamosite-type Phanerozoic ooidal ironstones. *Ore Geology Reviews*, *28*(2), 235–249. https://doi.org/10.1016/j.oregeorev.2005.03.004

Mücke, A., & Farshad, F. (2005). Whole-rock and mineralogical composition of Phanerozoic ooidal ironstones: Comparison and differentiation of types and subtypes. *Ore Geology Reviews*, *26*(3–4), 227–262. https://doi.org/10.1016/j.oregeorev.2004.08.001

Müller, B., Granina, L., Schaller, T., Ulrich, A., & Wehrli, B. (2002). P, As, Sb, Mo, and other elements in sedimentary Fe/Mn layers of Lake Baikal. *Environmental Science & Technology*, *36*(3), 411–420. https://doi.org/10.1021/es010940z

Nesbitt, H. W., & Young, G. M. (1984). Prediction of some weathering trends of plutonic and volcanic rocks based on thermodynamic and kinetic considerations. *Geochimica et Cosmochimica Acta*, *48*(7), 1523–1534. https://doi.org/10.1016/0016-7037(84)90408-3

Nimmo, F., & Tanaka, K. (2005). Early crustal evolution of Mars. *Annual Review of Earth and Planetary Sciences*, *33*(1), 133–161. https://doi.org/10.1146/annurev.earth.33.092203.122637

Noda, N., Imamura, S., Sekine, Y., Kurisu, M., Fukushi, K., Terada, N., et al. (2019). Highly oxidizing aqueous environments on early Mars inferred from scavenging pattern of trace metals on manganese oxides. *Journal of Geophysical Research: Planets*, *124*(5), 1282–1295. https://doi.org/10.1029/2018JE005892

O'Connell-Cooper, C. D., Spray, J. G., Thompson, L. M., Gellert, R., Berger, J. A., Boyd, N. I., et al. (2017). APXS-derived chemistry of the Bagnold dune sands: Comparisons with Gale Crater soils and the global Martian average. *Journal of Geophysical Research: Planets*, *122*(12), 2623–2643. https://doi.org/10.1002/2017JE005268

Pattan, J. N., & Banakar, V. K. (1993). Rare earth element distribution and behaviour in buried manganese nodules from the Central Indian Basin. *Marine Geology*, *112*(1–4), 303–312. https://doi.org/10.1016/0025-3227(93)90175-U

Payré, V., Fabre, C., Cousin, A., Sautter, V., Wiens, R. C., Forni, O., et al. (2017). Alkali trace elements in Gale crater, Mars, with ChemCam: Calibration update and geological implications: Alkali Trace Elements with Chemcam. *Journal of Geophysical Research: Planets*, *122*(3), 650–679. https://doi.org/10.1002/2016JE005201

Pelowitz, D. (2005). MNCPX user's manual, version 2.5.0, LANL, Los Alamos, Technical report, LA-UR-05-0369.

Rampe, E. B., Bristow, T. F., Morris, R. V., Morrison, S. M., Achilles, C. N., Ming, D. W., et al. (2020). Mineralogy of vera Rubin Ridge from the Mars science laboratory CheMin instrument. *Journal of Geophysical Research: Planets*, *125*(9), e2019JE006306. https://doi.org/10.1029/2019JE006306

Rampe, E. B., Ming, D. W., Blake, D. F., Bristow, T. F., Chipera, S. J., Grotzinger, J. P., et al. (2017). Mineralogy of an ancient lacustrine mudstone succession from the Murray formation, Gale crater, Mars. *Earth and Planetary Science Letters*, *471*, 172–185. https://doi.org/10.1016/j.epsl.2017.04.021

Rapin, W., Dromart, G., Clark, B. C., Schieber, J., Kite, E. S., Kah, L. C., et al. (2023). Sustained wet–dry cycling on early Mars. *Nature*, *620*(7973), 299–302. https://doi.org/10.1038/s41586-023-06220-3

Rapin, W., Dromart, G., Rubin, D., Deit, L. L., Mangold, N., Edgar, L. A., et al. (2021). Alternating wet and dry depositional environments recorded in the stratigraphy of Mount Sharp at Gale crater, Mars. *Geology*, *49*(7), 842–846. https://doi.org/10.1130/G48519.1

Rapin, W., Dromart, G., Schieber, J., Clark, B. C., Kah, L., Rubin, D., et al. (2023). Not always wet: An aridification sequence in the orbital clay-sulfate transition of Aeolis Mons. In *Presented at the 54th lunar and planetary science conference, the woodlands, TX, abstract# 2085*.

Reineck, H.-E., & Singh, I. B. (1980). *Depositional sedimentary environments*. Springer Berlin Heidelberg. https://doi.org/10.1007/978-3-642-81498-3

Roberts, A., Gupta, S., Banham, S. G., Cowart, A., Edgar, L. A., Rapin, W., et al. (2025). Paleo-Scours within the layered sulfate-bearing unit at Gale Crater, Mars: Evidence for intense wind erosion. *Journal of Geophysical Research: Planets*, *130*(5), e2024JE008680. https://doi.org/10.1029/2024JE008680

Rossmann, R., & Callender, E. (1968). Manganese nodules in Lake Michigan. *Science*, *162*(3858), 1123–1124. https://doi.org/10.1126/science.162.3858.1123

Salama, W., El Aref, M., & Gaupp, R. (2012). Mineralogical and geochemical investigations of the Middle Eocene ironstones, El Bahariya Depression, Western Desert, Egypt. *Gondwana Research*, *22*(2), 717–736. https://doi.org/10.1016/j.gr.2011.11.011

Schieber, J., Bish, D., Coleman, M., Reed, M., Hausrath, E. M., Cosgrove, J., et al. (2017). Encounters with an unearthly mudstone: Understanding the first mudstone found on Mars. *Sedimentology*, *64*(2), 311–358. https://doi.org/10.1111/sed.12318

Schoettle, M., & Friedman, G. M. (1971). Fresh water iron-manganese nodules in Lake George, New York. *Geological Society of America Bulletin*, *82*(1), 101. https://doi.org/10.1130/0016-7606(1971)82[101:FWINIL]2.0.CO;2

Schröder, S., Rammelkamp, K., Hansen, P. B., Seel, F., Cousin, A., Forni, O., et al. (2023). Semiquantitative analysis of ChemCam and SuperCam LIBS data with spectral unmixing. In *Presented at the 54th lunar and planetary science conference, the woodlands, TX, abstract 2014*.

Schwertmann, U., & Fanning, D. S. (1976). Iron-manganese concretions in hydrosequences of soils in loess in Bavaria. *Soil Science Society of America Journal*, *40*(5), 731–738. https://doi.org/10.2136/sssaj1976.03615995004000050054x

Siehl, A., & Thein, J. (1989). Minette-type ironstones. *Geological Society, London, Special Publications*, *46*(1), 175–193. https://doi.org/10.1144/GSL.SP.1989.046.01.16

Sleep, N. H., Meibom, A., Fridriksson, T., Coleman, R. G., & Bird, D. K. (2004). H2-rich fluids from serpentinization: Geochemical and biotic implications. *Proceedings of the National Academy of Sciences*, *101*(35), 12818–12823. https://doi.org/10.1073/pnas.0405289101

Sozanski, A. G., & Cronan, D. S. (1979). Ferromanganese concretions in Shebandowan Lakes, Ontario. *Canadian Journal of Earth Sciences*, *16*(1), 126–140. https://doi.org/10.1139/e79-012

Suess, E., & Djafari, D. (1977). Trace metal distribution in Baltic Sea ferromanganese concretions: Inferences on accretion rates. *Earth and Planetary Science Letters*, *35*(1), 49–54. https://doi.org/10.1016/0012-821X(77)90027-9

Suhr, N., Schoenberg, R., Chew, D., Rosca, C., Widdowson, M., & Kamber, B. S. (2018). Elemental and isotopic behaviour of Zn in Deccan basalt weathering profiles: Chemical weathering from bedrock to laterite and links to Zn deficiency in tropical soils. *Science of the Total Environment*, *619–620*, 1451–1463. https://doi.org/10.1016/j.scitotenv.2017.11.112

Sun, V. Z., Stack, K. M., Kah, L. C., Thompson, L., Fischer, W., Williams, A. J., et al. (2019). Late-stage diagenetic concretions in the Murray formation, Gale crater, Mars. *Icarus*, *321*, 866–890. https://doi.org/10.1016/j.icarus.2018.12.030

Swanner, E., & Gasda, P. (2025). Compiled literature chemistry and Gale crater, Mars data for the paper "Elucidating the mineralogy of terrestrial manganese minerals using laser-induced breakdown spectroscopy with relevance for Gale crater, Mars." [Dataset]. *Zenodo*. https://doi.org/10.5281/ZENODO.15425479

Swanson, C. O. (1923). The origin, distribution and composition of laterite. *Journal of the American Ceramic Society*, *6*(12), 1248–1260. https://doi.org/10.1111/j.1151-2916.1923.tb17709.x

Szymański, W., & Skiba, M. (2013). Distribution, morphology, and chemical composition of Fe-Mn nodules in albeluvisols of the carpathian foothills, Poland. *Pedosphere*, *23*(4), 445–454. https://doi.org/10.1016/S1002-0160(13)60037-5

Szymański, W., Skiba, M., & Błachowski, A. (2014). Mineralogy of Fe–Mn nodules in Albeluvisols in the Carpathian Foothills, Poland. *Geoderma*, *217–218*, 102–110. https://doi.org/10.1016/j.geoderma.2013.11.008

Takahashi, Y., Manceau, A., Geoffroy, N., Marcus, M. A., & Usui, A. (2007). Chemical and structural control of the partitioning of Co, Ce, and Pb in marine ferromanganese oxides. *Geochimica et Cosmochimica Acta*, *71*(4), 984–1008. https://doi.org/10.1016/j.gca.2006.11.016

Tardy, Y., & Nahon, D. (1985). Geochemistry of laterites, stability of Al-goethite, Al-hematite, and Fe (super 3+) -kaolinite in bauxites and ferricretes; an approach to the mechanism of concretion formation. *American Journal of Science*, *285*(10), 865–903. https://doi.org/10.2475/ajs.285.10.865

Taylor, G. J. (2013). The bulk composition of Mars. *Geochemistry*, *73*(4), 401–420. https://doi.org/10.1016/j.chemer.2013.09.006

Tebo, B. M., Bargar, J. R., Clement, B. G., Dick, G. J., Murray, K. J., Parker, D., et al. (2004). Biogenic manganese oxides: Properties and mechanisms of Formation. *Annual Review of Earth and Planetary Sciences*, *32*(1), 287–328. https://doi.org/10.1146/annurev.earth.32.101802.120213

Thompson, L. M., Berger, J. A., Spray, J. G., Fraeman, A. A., McCraig, M. A., O'Connell-Cooper, C. D., et al. (2020). APXS-Derived compositional characteristics of vera Rubin Ridge and murray Formation, gale crater, Mars: Geochemical implications for the origin of the Ridge. *Journal of Geophysical Research: Planets*, *125*(10), e2019JE006319. https://doi.org/10.1029/2019JE006319

Thompson, L. M., Spray, J. G., VanBommel, S. J., O'Connell-Cooper, C. D., Berger, J. A., Gellert, R., et al. (2024). Amapari marker band, gale crater, Mars: Event horizon with highest bedrock iron and zinc concentrations detected by curiosity's alpha particle X-Ray spectrometer. *Geophysical Research Letters*, *51*(23), e2024GL111113. https://doi.org/10.1029/2024GL111113

Thorpe, M. T., Bristow, T. F., Rampe, E. B., Tosca, N. J., Grotzinger, J. P., Bennett, K. A., et al. (2022). Mars science laboratory CheMin data from the Glen Torridon Region and the significance of lake-groundwater interactions in interpreting mineralogy and sedimentary history. *Journal of Geophysical Research: Planets*, *127*(11), e2021JE007099. https://doi.org/10.1029/2021JE007099

Treiman, A. H., Lanza, N. L., VanBommel, S., Berger, J., Wiens, R., Bristow, T., et al. (2023). Manganese-Iron phosphate nodules at the groken site, gale crater, Mars. *Minerals*, *13*(9), 1122. https://doi.org/10.3390/min13091122

Trolard, F., Bourrie, G., Jeanroy, E., Herbillon, A. J., & Martin, H. (1995). Trace metals in natural iron oxides from laterites: A study using selective kinetic extraction. *Geochimica et Cosmochimica Acta*, *59*(7), 1285–1297. https://doi.org/10.1016/0016-7037(95)00043-y

Tsikos, H., & Moore, J. M. (1997). Petrography and geochemistry of the Paleoproterozoic Hotazel Iron-Formation, Kalahari manganese field, South Africa; implications for Precambrian manganese metallogenesis. *Economic Geology*, *92*(1), 87–97. https://doi.org/10.2113/gsecongeo.92.1.87

Tutolo, B. M., Hausrath, E. M., Kite, E. S., Rampe, E. B., Bristow, T. F., Downs, R. T., et al. (2025). Carbonates identified by the Curiosity rover indicate a carbon cycle operated on ancient Mars. *Science*, *388*(6744), 292–297. https://doi.org/10.1126/science.ado9966

VanBommel, S. J., Berger, J. A., Gellert, R., O'Connell-Cooper, C. D., McCraig, M. A., Thompson, L. M., et al. (2023). Elemental composition of manganese- and phosphorus-rich nodules in the Knockfarril Hill member, Gale crater, Mars. *Icarus*, *392*, 115372. https://doi.org/10.1016/j.icarus.2022.115372

VanBommel, S. J., Gellert, R., Berger, J. A., Campbell, J. L., Thompson, L. M., Edgett, K. S., et al. (2016). Deconvolution of distinct lithology chemistry through oversampling with the Mars Science Laboratory Alpha Particle X-Ray Spectrometer. *X-Ray Spectrometry*, *45*(3), 155–161. https://doi.org/10.1002/xrs.2681

VanBommel, S. J., Gellert, R., Berger, J. A., McCraig, M. A., O'Connell-Cooper, C. D., Thompson, L. M., et al. (2022). Constraining the chemical depth profile of a manganese-rich surface layer in Gale crater, Mars. *Spectrochimica Acta Part B: Atomic Spectroscopy*, *191*, 106410. https://doi.org/10.1016/j.sab.2022.106410

VanBommel, S. J., Gellert, R., Berger, J. A., Yen, A. S., & Boyd, N. I. (2019). Mars Science Laboratory Alpha Particle X-ray spectrometer trace elements: Situational sensitivity to Co, Ni, Cu, Zn, Ga, Ge, and Br. *Acta Astronautica*, *165*, 32–42. https://doi.org/10.1016/j.actaastro.2019.08.026

Vasavada, A. R. (2022). Mission overview and scientific contributions from the Mars science laboratory curiosity rover after eight years of surface operations. *Space Science Reviews*, *218*(3), 14. https://doi.org/10.1007/s11214-022-00882-7

Von Stackelberg, U. (1997). Growth history of manganese nodules and crusts of the Peru Basin. *Geological Society, London, Special Publications*, *119*(1), 153–176. https://doi.org/10.1144/GSL.SP.1997.119.01.11

Wang, A., Kuebler, K. E., Jolliff, B. E., & Haskin, L. A. (2004). Raman spectroscopy of Fe-Ti-Cr-oxides, case study: Martian meteorite EETA79001. *American Mineralogist*, *89*(5–6), 665–680. https://doi.org/10.2138/am-2004-5-601

Weitz, C. M., Lewis, K. W., Bishop, J. L., Thomson, B. J., Arvidson, R. E., Grant, J. A., et al. (2022). Orbital observations of a marker horizon at Gale Crater. *Journal of Geophysical Research: Planets*, *127*(4), e2022JE007211. https://doi.org/10.1029/2022JE007211

Wiens, R. (2021a). MSL ChemCam laser induced breakdown spectrometer EDR v1.0 [Dataset]. *NASA Planetary Data System*. https://doi.org/10.17189/1519439

Wiens, R. (2021b). MSL ChemCam remote micro imaging camera EDR V1.0 [Dataset]. *NASA Planetary Data System*. https://doi.org/10.17189/1519456

Wiens, R. (2021c). MSL mars ChemCam libs spectra 4/5 RDR V1.0 [Dataset]. *NASA Planetary Data System*. https://doi.org/10.17189/1519485

Wiens, R. (2021d). MSL MARS ChemCam remote micro-imager camera 5 RDR V1.0 [Dataset]. *NASA Planetary Data System*. https://doi.org/10.17189/1519494

Wiens, R. C., Maurice, S., Barraclough, B., Saccoccio, M., Barkley, W. C., Bell, J. F., et al. (2012). The ChemCam instrument suite on the Mars Science Laboratory (MSL) Rover: Body unit and combined System tests. *Space Science Reviews*, *170*(1–4), 167–227. https://doi.org/10.1007/s11214-012-9902-4

Wordsworth, R., Knoll, A. H., Hurowitz, J., Baum, M., Ehlmann, B. L., Head, J. W., & Steakley, K. (2021). A coupled model of episodic warming, oxidation and geochemical transitions on early Mars. *Nature Geoscience*, *14*(3), 127–132. https://doi.org/10.1038/s41561-021-00701-8